Journal of Electronics Cooling and Thermal Control, 2024, 13, 1-34
https://www.scirp.org/journal/jectc
ISSN Online: 2162-6170
ISSN Print: 2162-6162

Investigation of Liquid Cooling Plate for Server CPUs Based on Topology Optimization

Guijun Ai, Yingying Luo, Wei Su*

Department of Applied Mechanics and Engineering, Shenzhen Campus, Sun Yat-sen University, Shenzhen, China
Email: *suwei@mail.sysu.edu.cn

How to cite this paper: Ai, G.J., Luo, Y.Y. and Su, W. (2024) Investigation of Liquid Cooling Plate for Server CPUs Based on Topology Optimization. *Journal of Electronics Cooling and Thermal Control*, **13**, 1-34.
https://doi.org/10.4236/jectc.2024.131001

Received: February 25, 2024
Accepted: March 26, 2024
Published: March 29, 2024

Abstract

In this study, a microchannel liquid cooling plate (LCP) is proposed for Intel Xeon 52.5 mm * 45 mm packaged architecture processors based on topology optimization (TO). Firstly, a mathematical model for topology optimization design of the LCP is established based on heat dissipation and pressure drop objectives. We obtain a series of two-dimensional (2D) topology optimization configurations with different weighting factors for two objectives. It is found that the biomimetic phenomenon of the topologically optimized flow channel structure is more pronounced at low Reynolds numbers. Secondly, the topology configuration is stretched into a three-dimensional (3D) model to perform CFD simulations under actual operating conditions. The results show that the thermal resistance and pressure drop of the LCP based on topology optimization achieve a reduction of approximately 20% - 50% compared to traditional serpentine and microchannel straight flow channel structures. The Nusselt number can be improved by up to 76.1% compared to microchannel straight designs. Moreover, it is observed that under high flow rates, straight microchannel LCPs exhibit significant backflow, vortex phenomena, and topology optimization structures LCPs also tend to lead to loss of effectiveness in the form of tree root-shaped branch flows. Suitable flow rate ranges for LCPs are provided. Furthermore, the temperature and pressure drop of experimental results are consistent with the numerical ones, which verifies the effectiveness of performance for topology optimization flow channel LCP.

Keywords

CPU, Sever, Data Center, Topology Optimization, Liquid Cooling Plate

1. Introduction

With the rapid development of global artificial intelligence (AI) technology and the digital economy, cooling technology is more and more employed to meet the

needs of facilities with a high power density and computing power, in terms of heat dissipation. At the same time, under the macro situation of "carbon neutrality," government departments have increasingly high requirements for Power Usage Effectiveness (PUE) [1] [2] of data centers. The design of the flow channel structure of the cold plate, in data center servers, is directly associated with the heat dissipation performance of the liquid cooling system and the power consumption of the pump, among other factors, making it a mainstream technology. In particular, optimizing the flow channel structure to reduce the overall pressure drop of the cold plate can reduce pump power and ultimately reduce data center energy consumption [3]. Therefore, the optimization of the cold plate flow channel structure is critical in improving the performance of liquid cooling systems [4]. Traditional liquid cooling plates (LCPs) for server processors are designed with different flow channel structures, including serpentine channels, microchannels, and piano key channels. Although conventional flow channels can achieve good application results, their design methods are often subjective and lack a complete theoretical basis as guidance. Additionally, because of their regular flow channel structures, achieving an optimal solution is often challenging, resulting in either poor heat dissipation performance, high pressure drop dissipation, or both, in most cases.

Topology optimization (TO) is an engineering design optimization method aimed at achieving the optimal performance of predefined performance objectives by adjusting the material distribution or geometric shape of the structure. In topology optimization, by adjusting the design variables of the structure, the structure can achieve the best performance under certain constraint conditions. Topology optimization originated from the challenge of optimizing frame structures. Maxwell [5] first proposed the problem of designing the lightest truss structure under specific loads, marking the beginning of research on topology optimization methods. Subsequently, Michell [6] proposed the theory of frame optimization design, with the designed truss structures also known as Michell frames. Dorn [7] first applied numerical methods to truss design problems, greatly advancing the development of topology optimization research and laying the foundation for the expansion of topology optimization from discrete bodies to continuum bodies. Cheng and Olhoff [8] developed the minimum compliance topology optimization method, achieving optimal design of variable-thickness reinforced ribs, and introduced the concept of microstructures in their work, pioneering the topology optimization of continuum structures.

Bendsøe [9], Zhou [10], and Mlejnek [11] introduced the Solid Isotropic Material with Penalization (SIMP) method, which represents the material distribution of a structure as a continuous design variable and achieves lightweight design of structures by adjusting the material density. With the advancement of research work, the SIMP method is currently the mainstream method for topology optimization design.

Scholars have also conducted topological optimization work on air-cooled heat sinks. Joo, Lee, and Kim [12] studied the shape effect on natural convection,

finding that optimizing heat sink topology led to a 15% decrease in thermal resistance and a 26% lower material weight compared to traditional designs. You [13] used a Logistic classification model for heat transfer coefficients, resulting in a successful application of topological optimization for structural fins. Through numerical simulations, a 5.9˚C temperature decrease in the heat sink baseplate was achieved while maintaining the flow resistance under 13.5 W power. Khan, Ullah, and Nawaz [14] established an active heat sink model consisting of a 9020 Fan and an arc-shaped heat sink. With the objective of minimizing material consumption, material cost reduction optimization was carried out based on the arc-shaped heat sink through topological optimization, resulting in a 13% reduction in material cost. These scholars conducted topological optimization designs on air-cooled heat sinks for natural or forced convection, simplifying complex convective heat transfer. They adopted a method of setting the convective heat transfer coefficient for the convective heat transfer boundary; in essence, it is actually a Robin boundary condition for thermal conduction topology optimization design, providing a convenient solution for convective heat transfer topological optimization designs.

Borrvall and Petersson [15] pioneered the field of topology optimization in fluid dynamics, focusing on Stokes flow and using the SIMP method of previous scholars to minimize energy loss in fluids as the optimization goal, proposing a method for topology optimization of flow in fluid. Subsequently, Evgrafov [16] and others expanded on the research by Borrvall and Petersson, considering the solid region as a porous medium and pointing out that even in design domains with extreme zero and infinite permeability, the topology optimization problem of Darcy-Stokes equations has optimal solutions.

Dede [17] innovatively integrated heat transfer model with fluid topology optimization by utilizing the COMSOL Multiphysics software along with the MMA method. This approach involved coupling physical processes such as conduction, convection-diffusion, and Navier-Stokes flow through a custom COMSOL/MATLAB script. Dede proposed that further research should concentrate on automated multi-objective weighting factors strategies, marking an intriguing starting point for future developments in fluid and heat transfer coupling. Yoon [18] used topology optimization for the heat transfer system with forced convection. By considering the heat flow coupled system, artificial damping force-inverse permeability was introduced into the N-S equation and interpolated. Similarly, interpolation of thermal conductivity, density, and specific heat capacity for topology optimization revealed the importance of balance between conduction and convection in the design of heat dissipation structures.

Based on a density-based SIMP method, Matsumori *et al.* [19] developed a topology optimization method for a fluid-solid-themal coupling problem of heat exchangers. They set the input power constant, and introduced an integral equation that determines the inlet pressure. The effects of the Reynolds number on the optimized topology structure and complexity of the flow channel were compared for temperature-dependent and temperature-independent heat sources.

Koga [20] highlighted the importance of a balance between conduction and convection in the design of heat dissipation structures, as well as the density design variables in topology optimization of conjugate heat transfer. Wei [21] proposed a technique for adaptive topology optimization in heat transfer structures, reducing numerical instabilities. They developed an iterative formula based on the Kuhn-Tucker optimality condition to establish an optimality criterion aiming to minimize heat dissipation. This approach included designing heat dissipation channels for 2D and 3D problems and validating the results against COMSOL outcomes. Cui [22] suggested that this coupling of fluid-solid-thermal and structural deformation be suitable for 2D and 3D models based on high temperature and pressure turbine casings. Hu [23] developed a mathematical model for fluid topology optimization using the density method to minimize energy dissipation. Programs were created and tested to analyze the impact of various parameters such as volume fraction, Reynolds number, and interpolation functions on the optimal channel structure. This study successfully determined suitable values for these topological parameters. Li *et al.* [24] optimized flow channel designs in LCPs for uniform and multiple heat source scenarios based on non-dimensional models. The study considered initial flow channel guesses, objective weighting factors, and Reynolds numbers. A flow channel structure with lower thermal resistance than a parallel one was achieved, followed by 3D simulation and experimental testing. Chen [25] developed a mathematical model for heat flow-coupled heat transfer optimization aiming to maximize heat transfer and minimize energy dissipation. A 2D flow channel model was created in COMSOL, and verified through 3D simulation and experiments, resulting in a cooling plate design with improved thermal resistance.

Zhao *et al.* [26] proposed a linearized Darcy model for modeling, and with the constraints of pressure drop and geometric length scale, clear and manufacturable cooling channel designs can be obtained. Studies of turbulence models have demonstrated that, despite the lack of inertial terms, the equivalent model can generally generate efficient cooling channel designs and provide satisfactory results. An [27] and Han [28] also conducted research on the topology optimization of cooling plates based on the Darcy model, and optimized and numerically verified the heat transfer and pressure drop performance of the optimized cooling plates.

Optimization of conjugate heat transfer topology can be employed to generate more efficient designs for LCP channels. However, there is a lack of feasible and widely applicable implementation methods, resulting in a high technical threshold for engineering applications [29]. Additionally, due to numerical instabilities, the fluid-structure-coupling topology optimization research conducted by the aforementioned scholars mostly consists of specific data combinations, some of which have too low velocity, low thermal conductivity settings, or mismatched dimensions, deviating from practical engineering applications.

With the development of the global low-carbon economy and progress in topology optimization research, in nearly three years, some scholars have consi-

dered applying topology optimization techniques to lithium-ion battery modules. Scholars such as Mo [30], Chen [31] [32], Wu [33], and Wang [34] have conducted research on the topology optimization methods for LCPs in lithium-ion battery modules. They have achieved better heat transfer performance and lower pressure drop dissipation in the design of LCP channels and have all indicated that density-based topology optimization methods are a suitable and efficient approach for battery thermal management.

The optimization of the conjugate heat transfer topology has been implemented to some degree in lithium-ion battery modules, yet the majority of these applications are confined to numerical methods and there is still a dearth of optimization examples for practical engineering purposes. Moreover, there is scarce research on the application of conjugate heat transfer TO techniques in liquid cooling technology for data center servers. We are convinced that in today's rapid development of artificial intelligence, with the increasing demand for computing power in data center servers and the low-carbon economy's requirement for energy efficiency, the optimal design of LCP channels is a crucial technological solution. As such, the research significance of conjugate heat transfer TO techniques in LCP design for server processors is considerable.

This paper researches the application of TO techniques for conjugate heat transfer on the LCP of Intel Xeon packaging architecture processors. First, a mathematical model for TO of the flow channel structure of the LCP is established using the SIMP density-based TO method. The model is based on the heat dissipation objective corresponding to the computational power requirements and the pressure drop dissipation objective for energy efficiency. Then, the TO parameters are set in the COMSOL program, and the program is run to obtain (2D) topology optimized configurations for different weighting factors on the objectives. The results of optimization of the topology are examined and contrasted. Furthermore, the topology optimized flow channel model is designed into a 3D engineering LCP. CFD simulations and corresponding experimental tests are conducted for the actual operating conditions of the LCP. Additionally, the fluid mechanics and heat transfer properties of the LCP are investigated, and the performance benefits of the topology-optimized LCP compared to the traditional serpentine and straight microchannel (1 mm microchannel and 2 mm microchannel) structures LCPs are evaluated.

2. Topology Optimization Design of LCP

2.1. Physical Model

In recent years Intel Xeon E series processors have been widely used as mainstream processors in foreign data centers such as Google Cloud, IBM, Amazon AWS, Microsoft Azure [35] [36], as well as Chinese data center servers from Huawei, Inspur, Lenovo, and Sugon [37] [38]. Recently, Intel Xeon D processors have also been widely used in edge computing and data centers [39]. As shown in **Figure 1**, this paper selects the packaging dimensions of the Intel Xeon E5

2600 series processor, 52.5 mm * 45 mm, as the design reference for defining the computational domain for topology optimization. The same design can also be applied to the latest Intel Xeon D processors. Figure 2 is a 2D plan defined for the TO design of the server CPU based on the above working conditions. The fluid inlet and outlet of the LCP are located on the same side, with the fluid entering from the upper left and flowing out from the lower left. This study chose a 2D topology optimization, with the inlet width L set to 6 mm. The size of the heat source is designed to fit the CPU and heat sink interface, set at 40 mm * 40 mm.

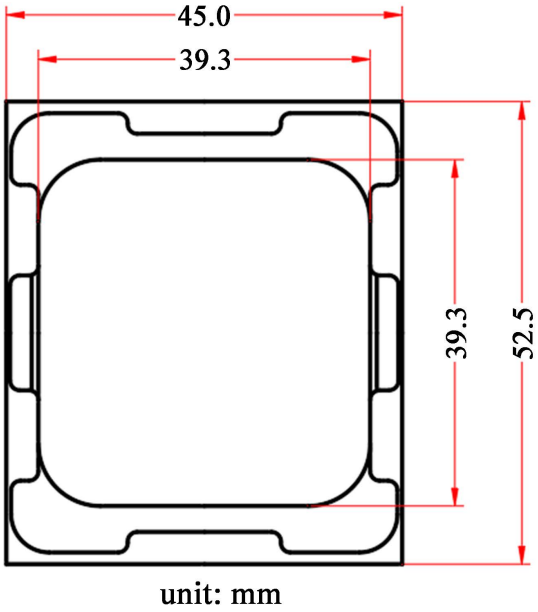

Figure 1. Architecture diagram of Intel Xeon E5 2600 series CPU [40].

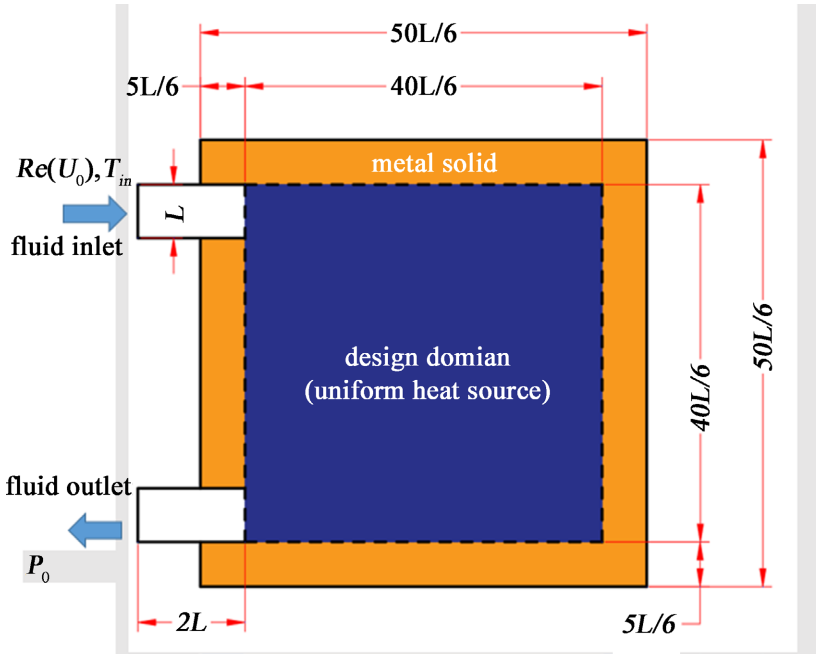

Figure 2. Topology optimization design domain.

The uniform heat source size is defined as the design domain, and to highlight the design focus, the design domain is set to be adiabatic at the contact wall with the metal solid. According to the working conditions, the fluid inlet temperature T_{in} is set to 25˚C, the Reynolds number is set to 200, and the outlet static pressure P_0 is set to 0 Pa. The heat source power is set to 50 W based on the Thermal Design Power (TDP) of the CPU, according to the specifications of the Intel Xeon processor.

2.2. Mathematical Model

2.2.1. Fluid Dynamics Governing Equations

The fluid working medium of the topology optimization study selects pure water H_2O, and the physical parameter of water at room temperature is heat capacity C_p, density ρ, thermal conductivity λ_f and viscosity μ. Reference [41] considers that the influence of temperature on fluid property parameters cannot be ignored when the temperature difference between the inlet and outlet is greater than 20˚C. According to [42], this paper suggests that the temperature difference between the inlet and outlet of the server LCP is much less than 20˚C, so the effect of the parameter changing with the temperature can be ignored. The topology optimization in this paper only studies the flow condition at steady state.

According to Brinkman penalty model [15], the distinction between fluid and solid can be achieved by defining the volume term F.

$$F = -\alpha \mathbf{u} \tag{1}$$

α is defined as the inverse permeability of the porous medium, where α equals 0, indicating no resistance for fluid flow in the porous medium, allowing fluid to pass through freely; whereas when α approaches infinity, the resistance of the porous medium to fluid flow becomes infinitely large, preventing fluid from passing through α is defined as a function of γ, denoted as $\alpha(\gamma)$, where a porous medium model is employed. γ represents the design variable of unit material density, with γ equal to 0 representing a solid unit, and γ equal to 1 representing a fluid unit. Therefore, the topological optimization of the fluid is achieved by varying the design of γ, which in turn changes the value of α to control the strength of Darcy permeability in local fluid regions. This ultimately determines the distribution of solids and fluids.

$$\alpha(\gamma) = \alpha_{\min} + (\alpha_{\max} - \alpha_{\min}) * q(1-\gamma)/(q+\gamma) \tag{2}$$

$$\alpha_{\min} = 0, \alpha_{\max} = \mu/(Da * L^2) \tag{3}$$

q represents the penalty factor, and for this topology optimization, its value is set at 0.1. Da is the dimensionless Darcy number, and according to [43], it is set to 10^{-4}.

The topology optimization Fluid dynamics equations are listed as below:

$$\nabla \cdot \mathbf{u} = 0 \tag{4}$$

$$\rho(\mathbf{u} \cdot \nabla)\mathbf{u} = -\nabla p + \mu \nabla^2 \mathbf{u} + \boldsymbol{F} \tag{5}$$

The boundary conditions are following.

$$\mathbf{u} = U_0 \text{ on } \Gamma_{in},\ U_0 = (Re * \mu)/(\rho * L),\ \mathbf{u} = 0 \text{ on } \Gamma_{wall},\ p = P_0 \text{ on } \Gamma_{out} \quad (6)$$

$\mathbf{u}$ is the velocity vector, p is the pressure term, Γ_{in}, Γ_{out}, Γ_{wall} is the inlet boundary, outlet boundary and wall boundary.

2.2.2. Heat Transfer Governing Equation

The heat transfer governing equations for solids and fluids are respectively as follows.

$$\lambda_s \nabla^2 T + Q = 0 \quad (7)$$

$$\rho(\mathbf{u} \cdot \nabla)\mathbf{u} = -\nabla p + \mu \nabla^2 \mathbf{u} + F \quad (8)$$

where Q is the Specific Volume Heat Dissipation $Q = TDP/V_{source}$,and V_{source} refers to the volume of the heat source.

In this paper, a customized material interpolation model is proposed.

$$\lambda(\gamma) = \lambda_s + (\lambda_f - \lambda_s)\gamma \quad (9)$$

Combining the above Equations (7)-(9), the following equation is obtained:

$$\gamma \rho C_p (\mathrm{u} \cdot \nabla) T = \lambda(\gamma) \nabla^2 T + (1 - \gamma) Q \quad (10)$$

The boundary condition is following

$$T = T_{in} \text{ on } \Gamma_{in} \quad (11)$$

When γ is 0, this heat transfer equation becomes Equation (7). When γ is 1, this equation becomes the fluid heat transfer Equation (8). λ_s is the thermal conductivity of the solid, which is set as 30 W/m·K in order to approximate the thermal conduction of metals as closely as possible.

Refer to **Figure 1**, assuming that the No. i (i = 1 2, 3, …, n) element of the design domain is a thermostatic heat source at T_q, after liquid cooling, its temperature decreases to T_i. Then the heat dissipated Q_i can be calculated as follows:

$$Q_i = H(T_q - T_i) \quad (12)$$

$$Q = \sum_{i=1}^{n} Q_i \quad (13)$$

T_q is set as 40˚C in all the elements, and the greater the temperature decrease, the greater the heat dissipation. H here refers to the heat generation coefficient, defined based on thermal design power (TDP) and design temperature difference as follows.

$$H = TDP/(V * \Delta T_{ave}) \quad (14)$$

ΔT_{ave} refers to the average temperature differences within the design domain for each unit.

$$\Delta T_{ave} = \sum_{i=1}^{n} (T_q - T_i)/n \quad (15)$$

The previous text mentioned that TDP is 50 W, and V is the volume stretched out by the LCP heat source, which is approximately 9.52381 × 10^{-6} m^3. According to the design goal, ΔT_{ave} is set to be 2˚C. Therefore, the calculated H is 2.625

$\times 10^6$ W/m^3.

2.2.3. Density Filter and Projection

To set the design domain mesh as a mapped quadrilateral type with a size of 3.75 $\times 10^{-4}$ m. Topology optimization can result in non-smooth patterns like stripes and checkerboards [44]. To address these phenomena, Helmholtz filtering can be used to obtain a smoother design variable γ_{fi} to improve the topology [45]. The filtering equation is as follows:

$$-R_{min}^2 \nabla^2 \gamma_{fi} + \gamma_{fi} = \gamma \tag{16}$$

R_{min} is the Helmholtz filtering radius, which is set to 5.625 $\times 10^{-4}$ m.

To eliminate the gray zone phenomenon at the solid-liquid boundary [46], a projection equation based on the hyperbolic tangent function is used

$$\hat{\gamma} = \frac{\tanh\left(\beta\left(\gamma_{fi} - \gamma_\beta\right)\right) + \tanh\left(\beta\gamma_\beta\right)}{\tanh\left(\beta\left(1 - \gamma_\beta\right)\right) + \tanh\left(\beta\gamma_\beta\right)} \tag{17}$$

$\hat{\gamma}$ is the filtered design variable γ_β refers to the projection point, β is the hyperbolic tangent projection slope, γ_β is set to 0.5.

2.2.4. Optimization Objective

Based on the increasing demand for computing power from servers, data centers, etc., this paper sets a heat dissipation objective. Referring to [19], the heat dissipation objective defined as the integral of the sum of heat dissipation of each unit in the design domain Ω, is obtained in an integral form.

$$\varphi_{th} = \int_\Omega \left(1 - \gamma\right) H\left(T_q - T\right) \mathrm{d}\Omega \tag{18}$$

Based on the requirement to reduce energy consumption by lowering PUE, the pressure drop dissipation objective can be rewritten as the total energy loss [43] [47] [48]:

$$\varphi_f = \int_\Omega \left(\frac{1}{2} \mu \left(\nabla \mathbf{u} + \nabla \mathbf{u}^{\mathrm{T}}\right) : \left(\nabla \mathbf{u} + \nabla \mathbf{u}^{\mathrm{T}}\right) + \alpha\left(\gamma\right) \mathbf{u} \cdot \mathbf{u} \right) \mathrm{d}\Omega \tag{19}$$

The units of heat dissipation objective and the pressure drop dissipation objective are not the same. The topology optimization of multiple objectives needs to be normalized to make the two objectives dimensionless.

$$J_{th} = \frac{\varphi_{th} - \varphi_{th\_min}}{\varphi_{th\_max} - \varphi_{th\_min}} \tag{20}$$

$$J_f = \frac{\varphi_f - \varphi_{f\_min}}{\varphi_{f\_max} - \varphi_{f\_min}} \tag{21}$$

$\varphi_{th\_max}, \varphi_{th\_min}$ are the normalized heat dissipation indices and are respectively set as 1.699 $\times 10^4$ W/m, 1.399 $\times 10^4$ W/m; $\varphi_{f\_max}, \varphi_{f\_min}$ are the normalized pressure drop dissipation indices and are respectively set as 9.5 $\times 10^{-4}$ W/m, 9.5 $\times 10^{-5}$ W/m.

Then the total objective of the topology optimization can be expressed as:

$$J = -w_{th} * J_{th} + w_f * J_f \tag{22}$$

$$w_{th} + w_f = 1 \tag{23}$$

w_{th} is the weighting factor of the normalized heat dissipation objective J_{th}, and w_f is the weighting factor of the normalized pressure drop dissipation J_f. The J_{th} needs to be maximized, while the J to be minimized. The two objectives are opposite, so the heat dissipation objective is added a minus to achieve unity.

2.2.5. Topology Optimization Mathematical Model

V_f is the maximum fluid volume fraction of the whole design domain, which is set to 0.5 here. Then the TO fraction controlling expression can be written as:

$$0 < \frac{\int_\Omega \gamma \mathrm{d}\Omega}{\int_\Omega 1 \mathrm{d}\Omega} \le V_f \tag{24}$$

To sum up, the TO mathematical model of the LCP can be expressed as:

find $\gamma_i \left(i = 1, 2, 3, \cdots, n\right)$

min $J = -w_{th} * J_{th} + w_f * J_f$

Subject to:

Equations (1)-(24)

$0 \le \gamma \le 1$.

2.3. Program and Algorithm

This study uses the topology optimization function in COMSOL to set up the model and parameters as described in section 2.2. The size of the quadrilateral mesh elements is set to L/16. Since **u**, p, T, and objective function J can only be implicitly expressed by design variable γ, sensitivity analysis using the adjoint variable method is required, referring to [24] [43]. The topology optimization uses the gradient-based optimization method SNOPT algorithm [49] [50] for calculations, with a maximum iteration of 300. The residual-iteration termination criterion for the objective function J is:

$$\left| J_{(k+1)} - J_k \right| < 10^{-6}$$

2.4. Topology Optimization Results with Different Weighting Factors

The w_{th} is sequentially set to 0.1, 0.3, 0.5 0.7, 0.9, and the penalty factor q or R_{min} is appropriately adjusted (Except for w_{th} = 0.5, which Use the settings from Section 2.3). And the results of the topology optimization are shown in **Figure 3**. It can be observed that when w_{th} is smaller and w_f is larger, the topology channels are thicker, with fewer branches, and the temperature distribution is relatively uneven. The temperature is higher in the two right corners, and the pressure in the design domain is relatively low. As w_{th} increases, the topology channels become finer and more widely distributed throughout the design domain. The temperature gradually becomes more uniform, but the pressure in the design domain also increases.

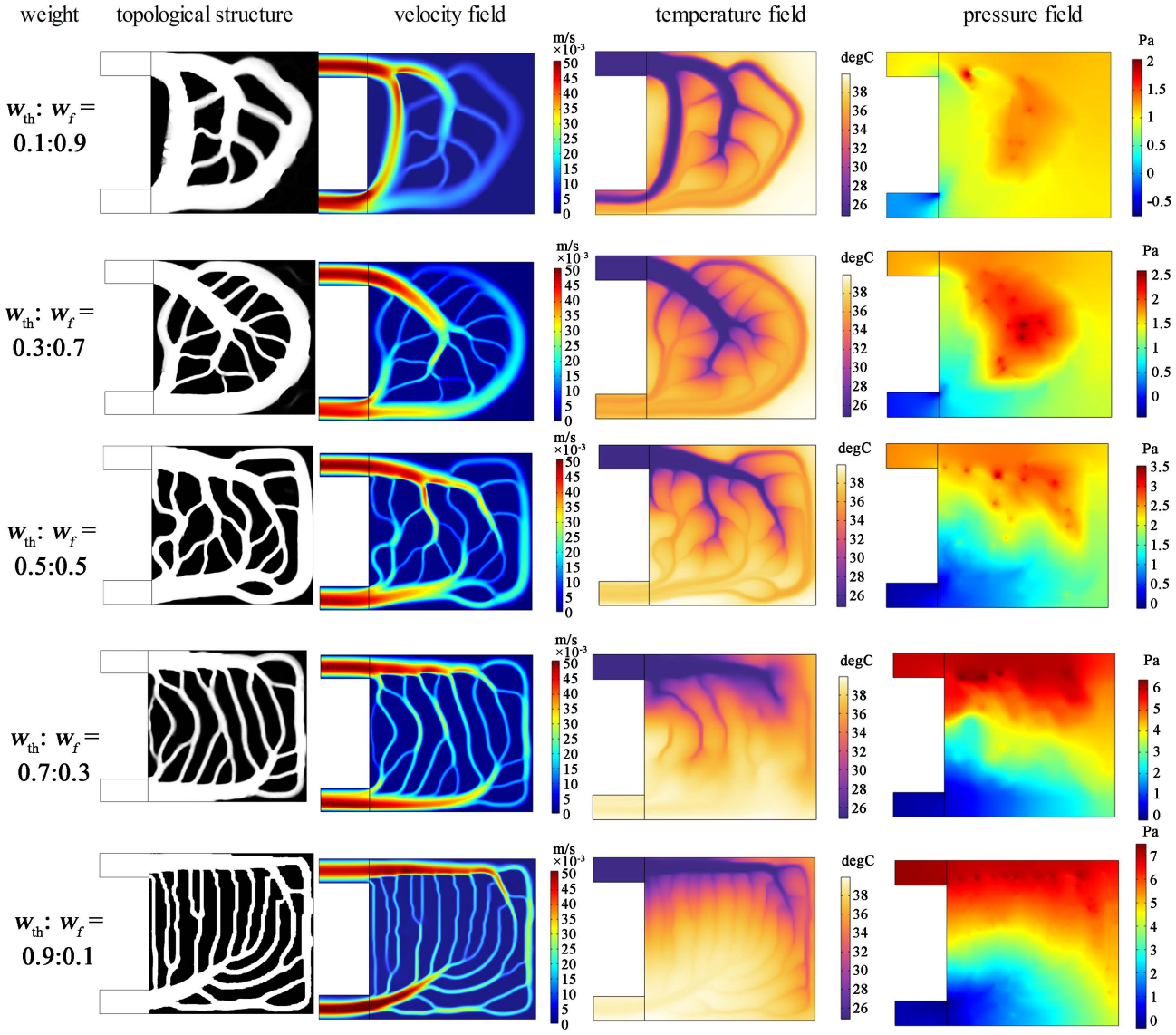

Figure 3. TO Results for different objective weighting factors.

Among the results with w_{th}:w_f = 0.1:0.9, the topology channel is the thickest, with the fewest branches and the worst temperature uniformity. However, the pressure is the lowest, with an inlet pressure of 1.05 Pa and a maximum pressure of 2.05 Pa at the first main branch. The topology results with w_{th}:w_f = 0.9:0.1 has the thinnest flow channels and the highest number of branches, resulting in the best temperature uniformity. However, the pressure is relatively high. The inlet pressure is 7.31 Pa, and the maximum pressure is 8.22 Pa. At several locations where the main flow channels in the designed domain divide into finer branches, the pressure is close to the maximum pressure.

The structure of the TO flow channels obtained from **Figure 3** resembles biological shapes, such as marine organisms and tree roots. This also indicates a coincidence between the results obtained through mathematical modeling and program calculations and the principles of biomimicry in nature.

In consideration of both the thermal performance and pressure drop losses, w_{th}:w_f = 0.5:0.5 TO flow channels structure has better comprehensive performance. This paper select the w_{th}:w_f = 0.5:0.5 TO result for the next step investigation: 3D design and CFD Numerical study for the TO LCP.

3. Numerical Investigation of LCPs with Different Channels

3.1. Computational Model

We stretch the solid part of the 2D topology configuration in the normal direction, and then form a 3D TO engineering and computational model (Figure 4). The 3D LCP design scheme is based on the numerical simulation of heat transfer and flow of LCPs with different channels. And the liquid cooling working medium is set as pure water H_2O. As a dummy heater to simulate the CPU thermal design power (*TDP*), the size of the ceramic heating plate is 40 mm * 40 m * 2 mm. Steady state analysis is utilized, and boundary conditions, heat source loads, and structural decomposition refer to Figure 4. Simulation analysis was conducted according to the cases in Table 1 to study the thermal performance and pressure drop dissipation of the LCP with four different channels (the

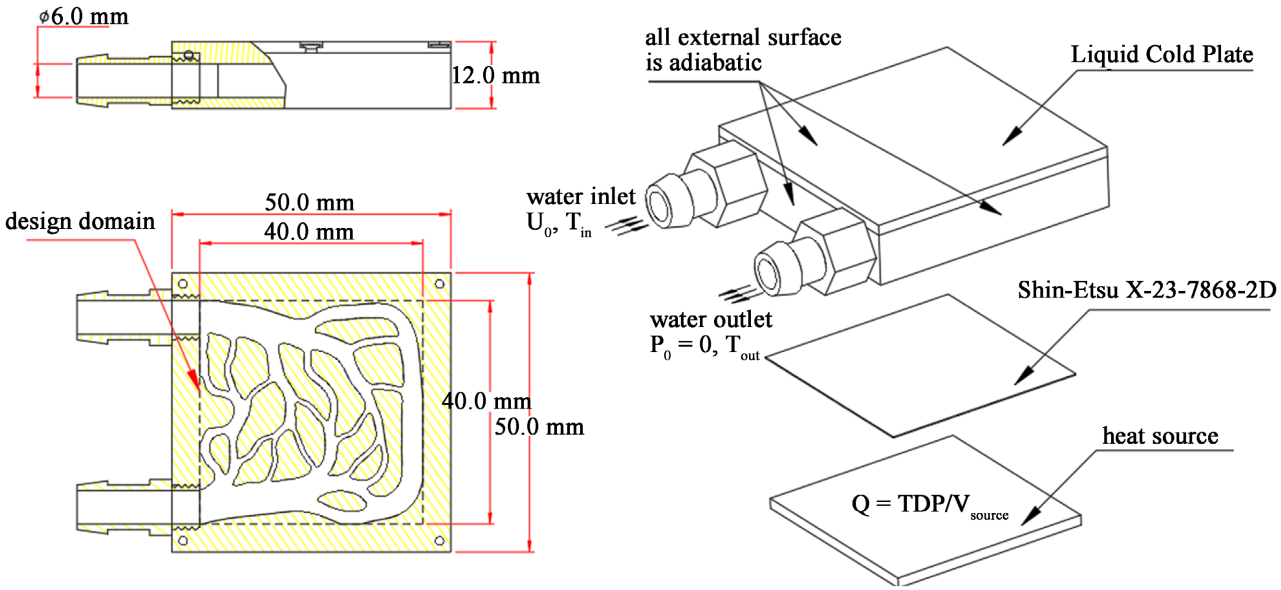

Figure 4. 3D engineering (left) and computational (right) model of LCP.

Table 1. CFD simulation CASEs.

Working condition	Flow rate (mL/min)	*TDP* (W)	T_{in} (˚C)	LCPs flow channel
CASE1	66	50	25	Serpentine type, 2 mm channel, 1 mm channel, $w_{th}:w_f = 0.5:0.5$
CASE2	250	126	35	Serpentine type, 2 mm channel, 1 mm channel, $w_{th}:w_f = 0.5:0.5$
Multi-flow rate CASEs	66, 100, 150	50	25	2 mm channel, $w_{th}:w_f = 0.5:0.5$
	200, 250, 300, 350, 400	126	35	

serpentine, 2 mm microchannel, 1 mm microchannel and w_{th}:w_f = 0.5:0.5 TO structural flow channel, as shown in Figure 5).

3.2. Governing Equations

The fluid dynamics equations and heat transfer governing equations are Equations (4), (5) and (8), eliminated the volume force term $\boldsymbol{F}$. The boundary conditions are Equation (6) and Equation (11). The average thermal resistance and maximum thermal resistance of 3D LCP are respectively calculated according to the following formula, whose units are both K/W [24] [51].

$$R_{th\_avg} = \frac{T_{ave} - T_{in}}{TDP} \tag{25}$$

$$R_{th\_max} = \frac{T_{max} - T_{in}}{TDP} \tag{26}$$

where T_{ave}, T_{max} is the average temperature and maximum temperature of the ceramic heat source.

The equivalent convection heat transfer coefficient of the LCP h_{avg} and Nusselt number Nu are calculated according to the following formulas [24] [33] [51].

$$h_{avg} = \frac{TDP}{A_{eff}\left(T_{w,avg} - T_{f,avg}\right)} \tag{27}$$

$$Nu = \frac{h_{avg} * D_h}{\lambda_f} \tag{28}$$

where A_{eff} is the contact area between the fluid and the solid wall, $T_{w,avg}$ is the average temperature of the wall, $T_{f,avg}$ is the average temperature of the fluid, and D_h is the hydraulic diameter, which is equal to L in this paper.

3.3. Meshing

Based on the finite volume method, Fluent has been widely applied in the simulation

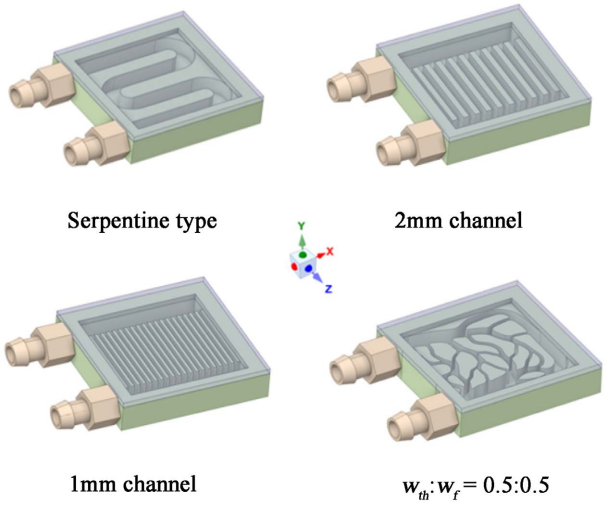

Figure 5. 3D computational models.

of flow and heat transfer in CPU coolers or LCPs [14] [52] [53]. This paper also employs Fluent for CFD simulation, Fluent-meshing is utilized for the Numerical simulation and the Poly-Hexco mesh is applied. Taking the topology structure LCP with w_{th}:w_f = 0.5:0.5 as an example, First, Mesh Sensitivity & Independence analysis was conducted, as shown in the **Figure 6**, when continuing to refine the grid, the maximum temperature T_{max} change and average temperature T_{ave} change of the heat source both do not exceed 0.05˚C, so we choose mesh quantity 2231637 scheme to ensure that the numerical analysis results are independent of the mesh. As shown in **Figure 7**, the final attained the mesh size for

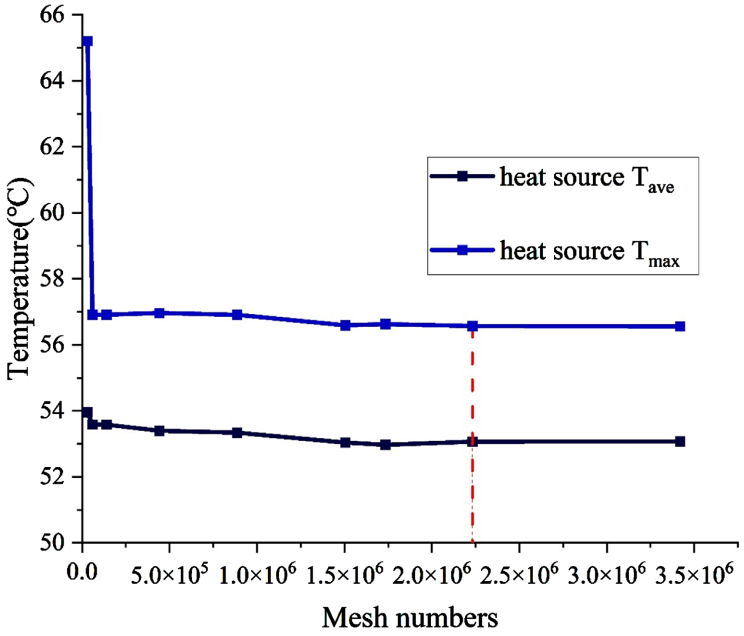

Figure 6. $w_{th} : w_f = 0.5 : 0.5$ TO LCP Mesh Sensitivity & Independence analysis.

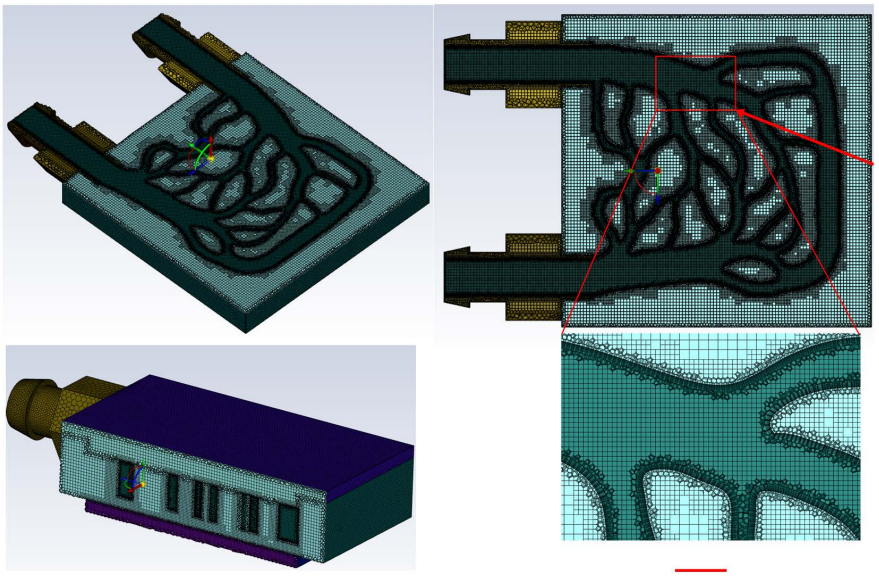

Figure 7. $w_{th} : w_f = 0.5 : 0.5$ TO liquid cold plate mesh diagram.

the critical areas such as the LCP and heat source is 0.25 mm. The maximum mesh size for other region is 2 mm. The overall mesh quality, judged by Orthogonal Quality, is above 0.3, and the Skewness is kept below 0.7. The meshing method for the other three LCPs with traditional flow channels follows the same settings as w_{th}:w_f = 0.5:0.5.

3.4. Simulation Settings

In Fluent, The numerical investigations are carried for laminar incompressible flows and steady state analysis, and the velocity of the inlet are expressed as fully developed speed expression. The flow material is pure water H_2O. Table 2 lists the physical properties of the other part materials. The interface thermal resistance is set to 10^{-4} K·m^2/W between the upper cover and main body of the LCPs. And the outer surface of the LCPs and heat source are set to be adiabatic. As is shown in Figure 8, five points are set on the bottom surface of the heat source, which locates respectively at the "center", "leftup", "leftdown", rightup", and "rightdown". To detect the simulation temperature data coordinates for the "center" point are (0, 0, 0), and for the "leftup" point it is (−15, 0, 15), the unit of the coordinates is mm. The others are distributed symmetrically.

3.5. Results and Discussion

3.5.1. CASE1 and CASE2 Results

Figure 9 is the temperature field at the center interface of the Z-axis in CASE1

Table 2. CFD Material property.

Part	Material	λ_s W/m·K	ρ Kg/m^3	C_p J/kg·K
heat source	Alumina ceramic	20	3970	765
connector	Brass	110	8400	385
thermal grease	Shin-EtsuX-23-7868-2 D	6.2	—	—
LCP	Al6063	202.4	2719	871

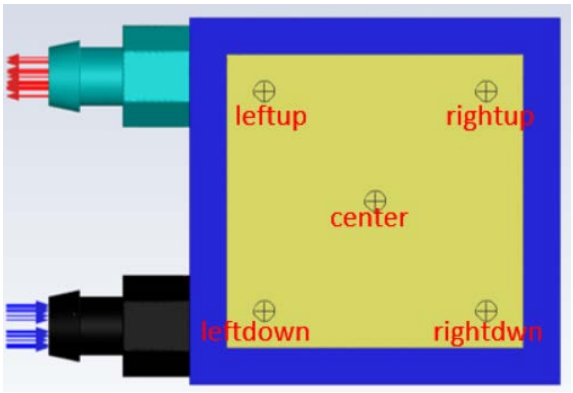

Figure 8. Location of the heat source temperature detection point.

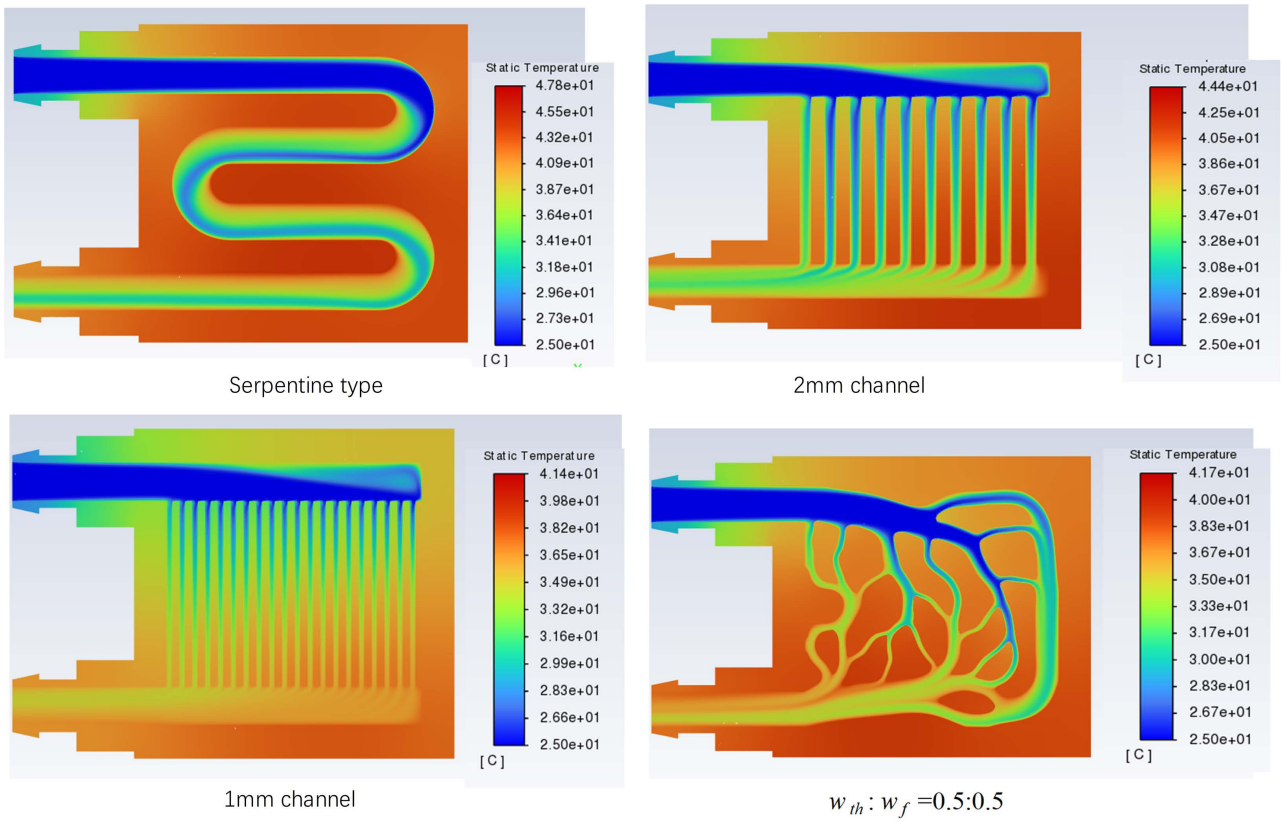

Figure 9. Temperature field of the Z-axis center section in CASE1 (66 mL/min, 50 W). w_{th}:w_f= 0.5:0.5.

(66 mL/min, 50 W). It is found that the maximum temperature of the LCP with the serpentine channel is 47.78˚C, which is in the center of the cold plate section. While those of the LCPs with 2 mm and 1 mm microchannel structure is 44.42˚C and 41.44˚C, respectively, which distributed in the lower right corner of the overhead direction because of heat accumulation. There are vortices and backflow in the right corners in both cases. In the TO LCP, and the highest temperature point is distributed in the "leftdown" position near the outlet, which is 41.66˚C.

Figure 10 is the temperature distribution of the bottom section of LCP with various flow channel structures in CASE2 (250 mL/min, 126 W). It is shown that the temperatures are highest in the upper right corner, 61.91˚C and 56.92˚C, respectively for LCPs with 2 mm and 1 mm microchannel channel. While the highest temperature point of the LCP with TO structure is at the outlet, which is 56.67˚C, and the temperature uniformity is better. Figure 11 is the velocity field distribution of the Z-axis center section of case 2 (250 mL/min, 126 W, T_{in} = 35˚C). As the flow rate increases, it is obvious to found the backflow, vortex in the upper right corner of LCPs with the traditional 2 mm microchannel, 1 mm microchannel, which to a certain extent increases the pressure loss. As can be seen from the pressure field contour in Figure 12, a large pressure is obvious in the case of the 2 mm microchannel and the 1 mm microchannel.

Based on the simulation results, the thermal performance comparison results are shown in Figures 13-15, in which the five points refer to locations at the

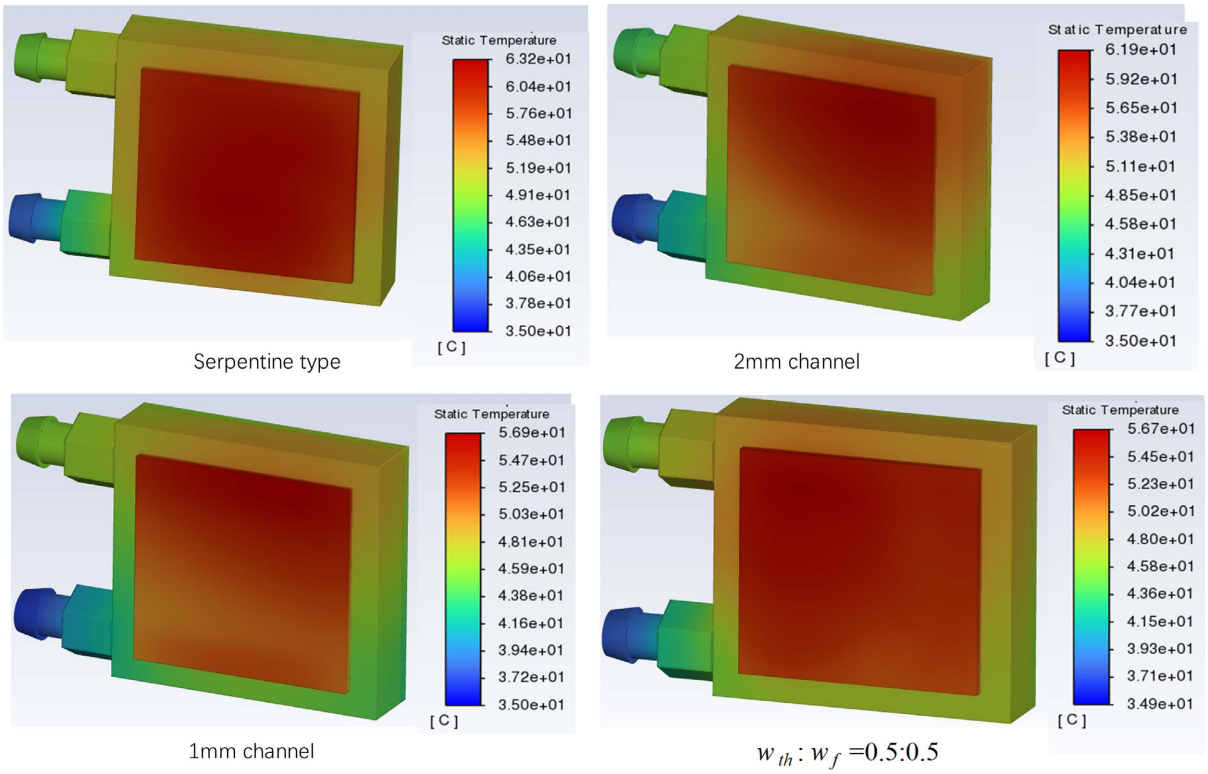

Figure 10. Temperature field on the bottom section in CASE2 (250 mL/min, 126 W).

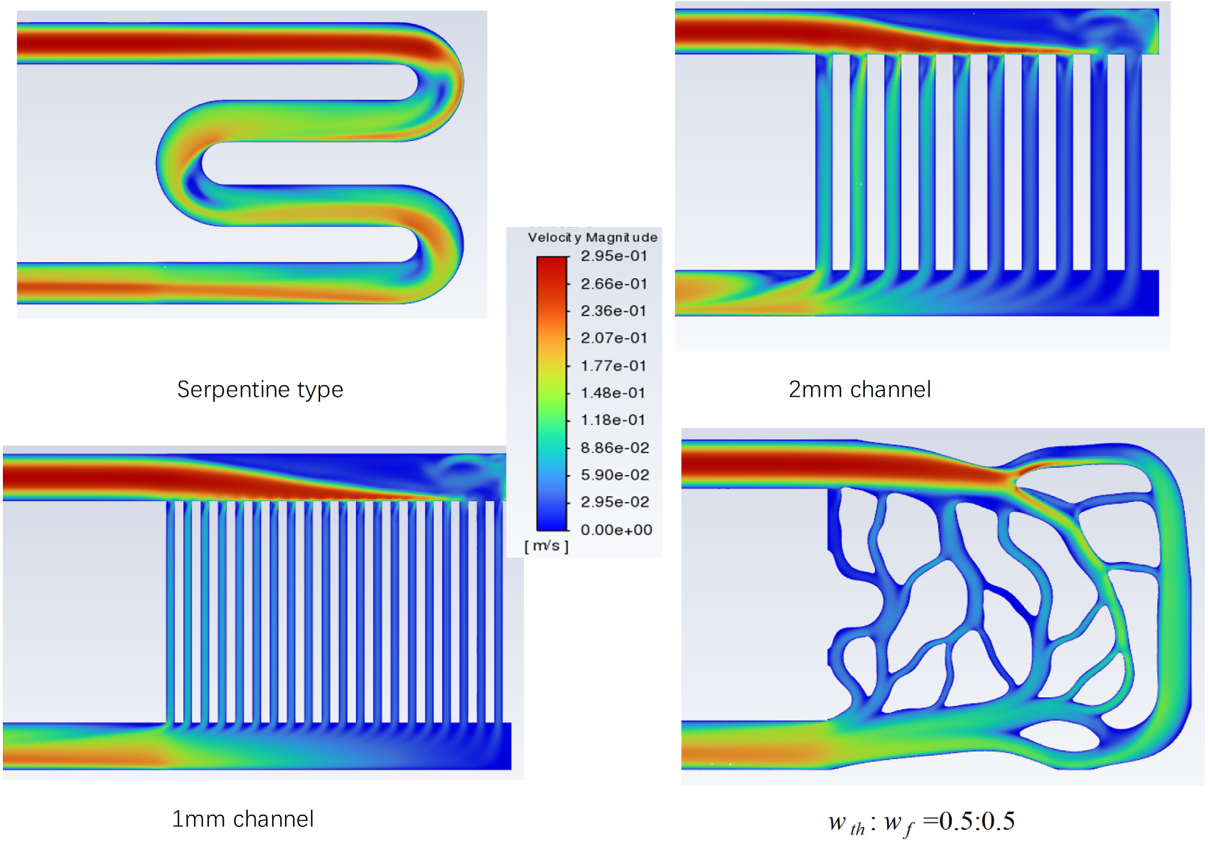

Figure 11. CASE2 (250 mL/min, 126 W) velocity field of the Z-axis center section.

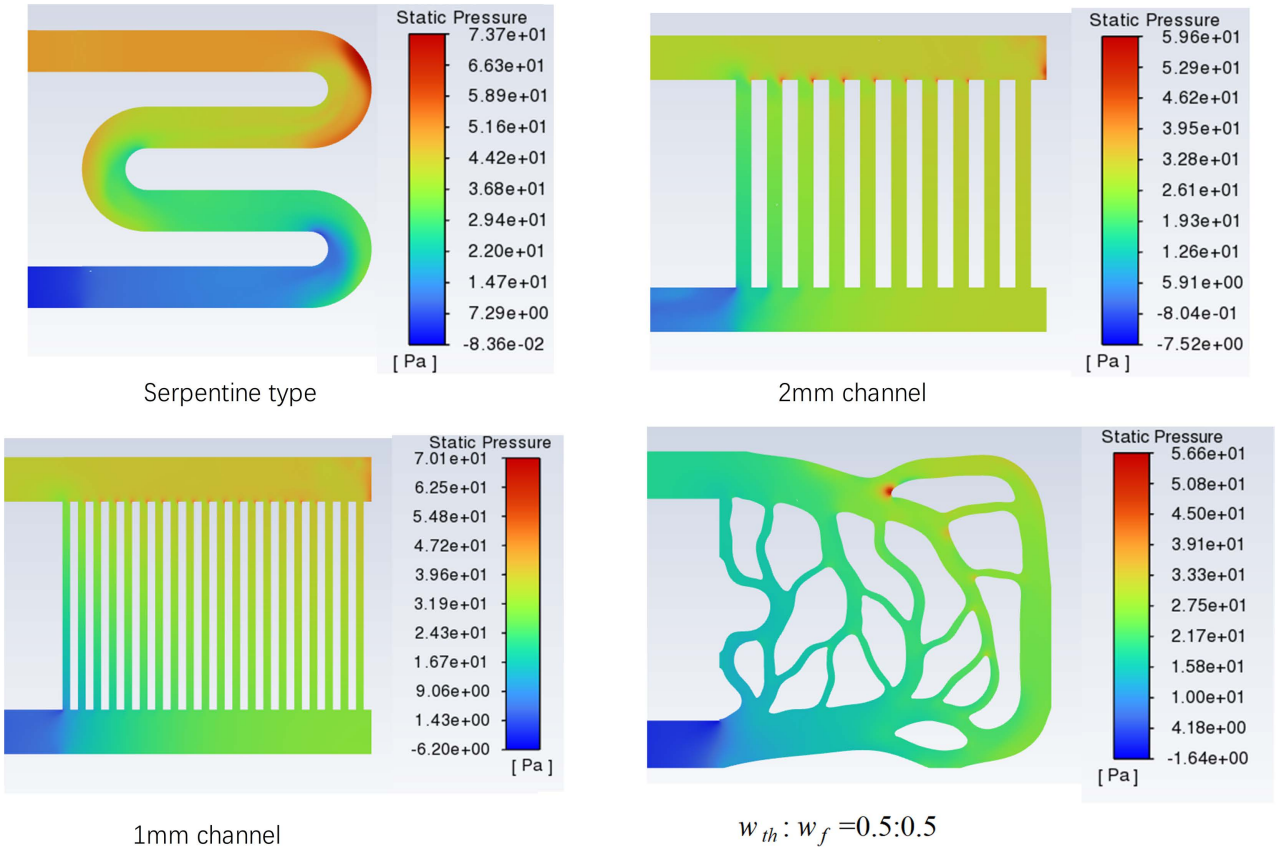

Figure 12. Pressure field of the Z-axis center section in CASE2 (250 mL/min, 126 W).

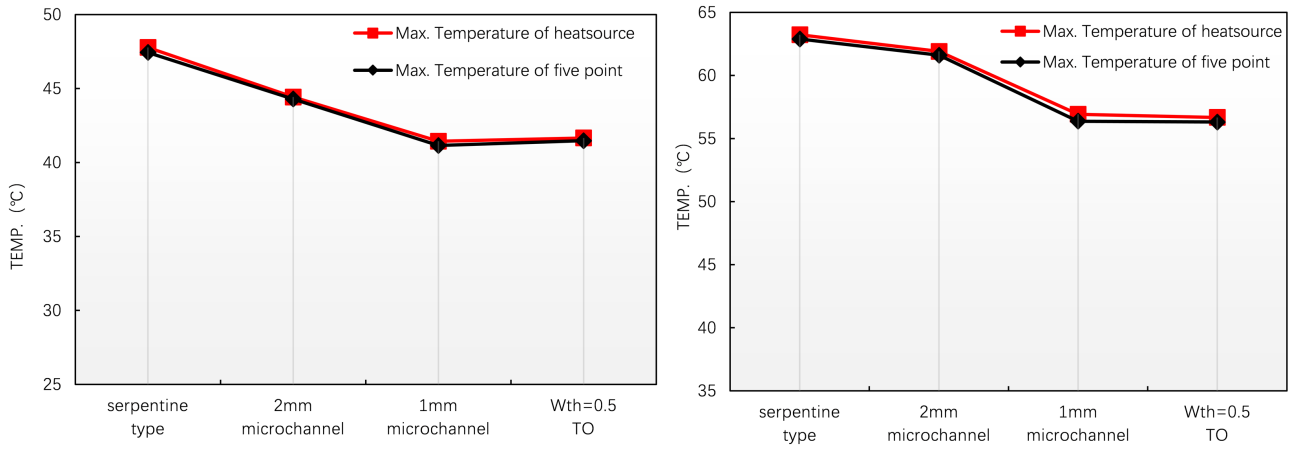

Figure 13. Maximum temperature of heat source for various flow channel structures in CASE1 (left) and CASE2 (right).

bottom of the heat source set in Figure 8. And the comparison of the pressure drop between the inlet and outlet of the liquid cold plate is obtained in Figure 16.

Under CASE1 (66 mL/min, 50 W), the TO flow channel liquid cold plate: compared with the traditional serpentine flow channel, maximum temperature of heat source is reduced by 6.1˚C, maximum thermal resistance is reduced by 26.9%, the *Nu* is increased by 40.9%, and the pressure loss is reduced by

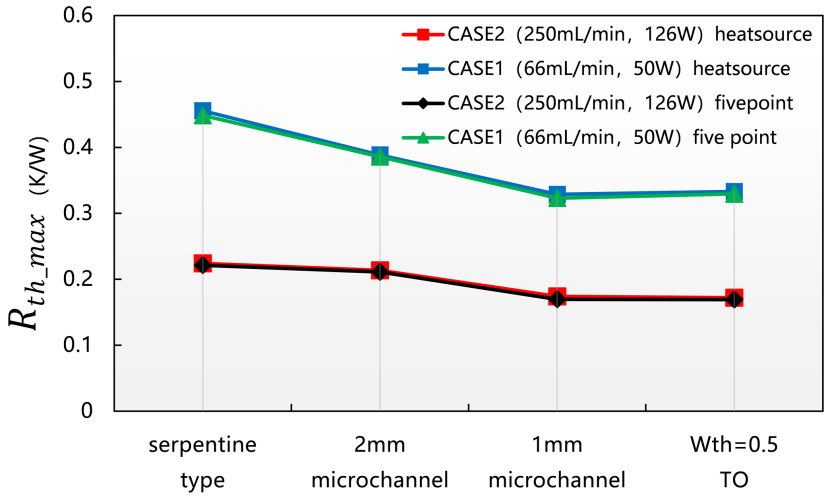

Figure 14. Thermal resistance of LCPs with various flow channel structures in CASE1 and CASE2.

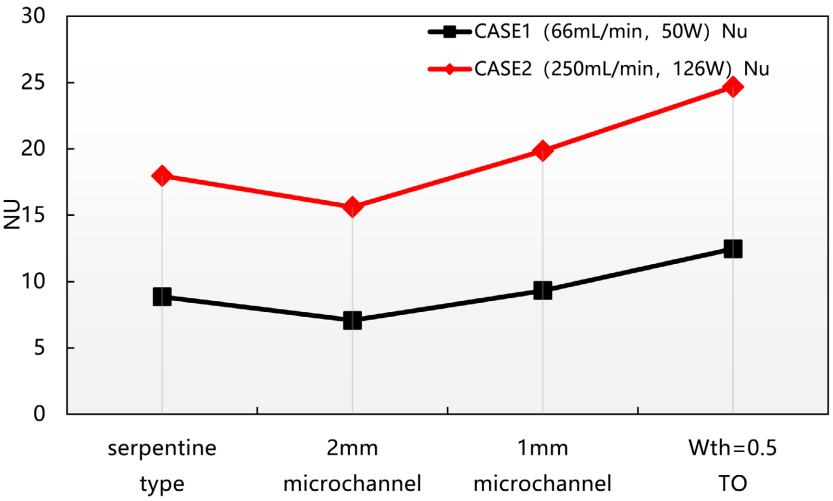

Figure 15. Nusselt number for LCPs with various flow channel structures in CASE1 and CASE2.

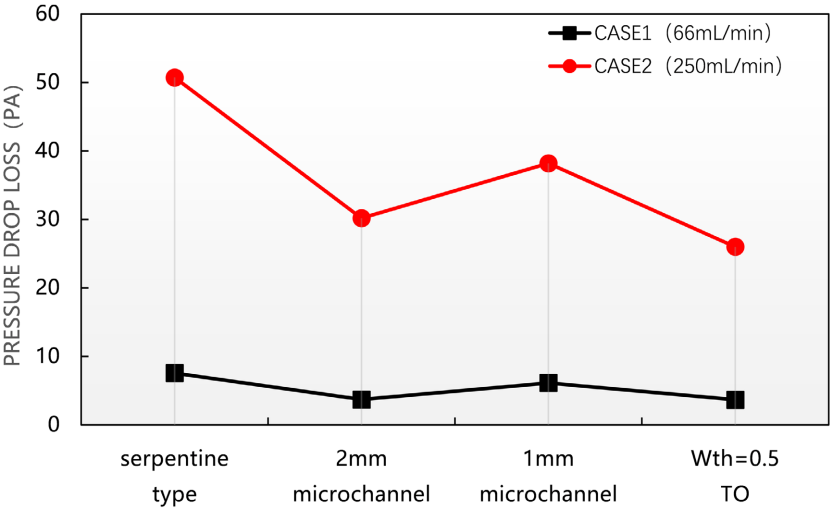

Figure 16. Pressure drop comparison for LCPs with various flow channel structures in CASE1 and CASE2.

51.3%; Compared with the 2 mm microchannel, the maximum temperature is reduced by 2.77˚C, the maximum thermal resistance is reduced by 14.3%, the *Nu* number is increased by 76.1%, and the pressure difference is nearly equal (difference of 0.675%); Compared with the 1 mm microchannel, the maximum temperature is nearly equal (difference 0.22˚C), but the convective heat transfer *Nu* is increased by 33.8%, and the pressure drop loss is reduced by 39.9%.

Under CASE2 (250 mL/min, 126 W), the TO liquid cold plate: compared with the traditional serpentine flow channel, the maximum temperature of the heat source is reduced by 6.5˚C, the maximum thermal resistance is reduced by 23.2%, the convective heat transfer Nu is increased by 37.2%, and the pressure loss is reduced by 48.7%. Compared with the 2 mm microchannel, the maximum temperature is reduced by 5.24˚C, maximum thermal resistance is reduced by 19.5%, the Nu is increased by 57.9%, and the pressure drop loss is reduced by about 13.9%. Compared with the 1 mm microchannel, the maximum temperature is comparable (0.25˚C difference), but the Nu is increased by 24.2%, and the pressure drop loss is reduced by about 31.9%. The highest temperature point of the serpentine flow channel is near the center point, the temperature maximum point of the 2 mm and 1 mm microchannels is at the rightdown point, and the temperature maximum point of the TO LCP is near the leftdown point.

To compare the temperature measurement results of the five temperature detection points set in Figure 8, the maximum temperature of these five points can be close to the maximum temperature of the heat source (the difference in CASE1 is not more than 0.3˚C, and the difference in CASE2 is not more than 0.6˚C), and the average temperature can also be close to the average temperature of the heat source (the difference in case 1 is less than 0.8˚C, and the difference in condition 2 is less than 1.1˚C). The temperature distribution of the five points can also reflect the temperature distribution of heat source. All these provide a reasonable basis for the location arrangement of experimental test detection points.

3.5.2. Multi-Flow Rate CASEs Results

Figure 17 compares the velocity vector diagrams of the TO flow channel and the 2 mm microchannel in LCPs at flow rates of 100 mL/min and 200 mL/min. The TO flow channel shows almost no backflow and vortex phenomena, while the topology optimized structure can avoid vortices and backflow to a large extent. However, for the 2 mm microchannel, as shown in Figure 18, there is backflow and vortices in the top right corner. At a flow rate of 100 mL/min, backflows and vortices occur at the 90-sharp turn of the microchannel, especially a relatively gentle large vortex at the upper right corner; At a flow rate of 200 mL/min, the vortices become turbulent; At a flow rate of 400 mL/min, the vortices become even more turbulent and the number of vortices increases significantly, resulting in increased energy dissipation. At low flow rates, the pressure drop loss between the 2 mm microchannel LCP and the TO LCP is approximately equal (the pressure drop difference is less than 0.7% at a flow rate of 66 mL/min). However, as

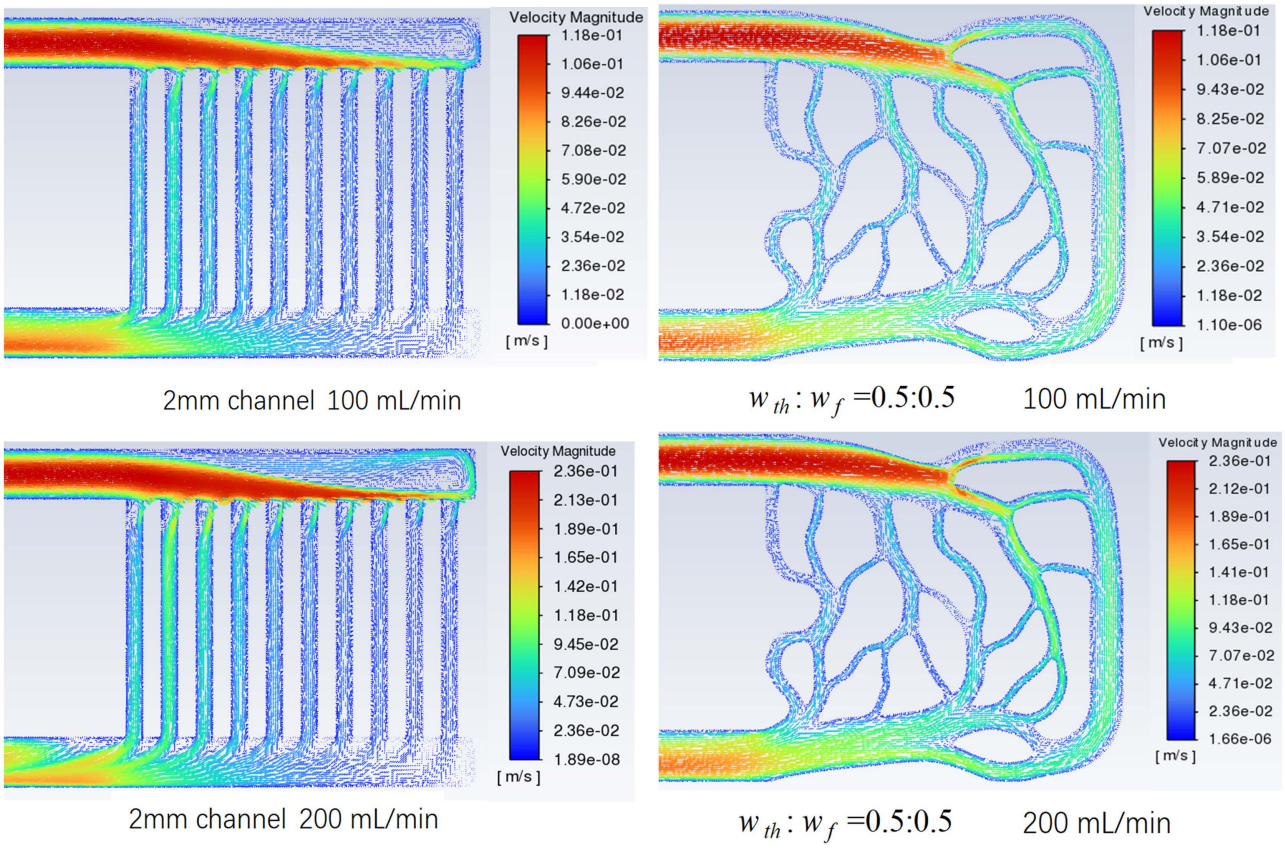

Figure 17. The velocity vector field of the Z-axis center section (100 mL/min, 200 mL/min)

the flow rate increases, the pressure drop loss of the 2 mm microchannel LCP becomes larger due to the increase in backflow and vortices. This trend becomes more pronounced with higher flow rates. At a flow rate of 400 mL/min, the pressure drop loss of the 2 mm microchannel LCP is 22% higher than that of the w_{th}:w_f = 0.5:0.5 TO LCP.

This study topologically designed the w_{th}:w_f = 0.5:0.5 TO LCP based on the Reynolds number 200, which corresponds to a flow rate of 66 mL/min (CASE1). It has been verified that it is also suitable for flow rates ranging from 66 mL/min to 350 mL/min. However, when the flow rate increases to a certain value (400 mL/min, corresponding to Reynolds number 1412), as shown in **Figure 19** the small branches in the red circle have very little fluid passing through, resulting in the failure of the root-like branching structure.

In conclusion, due to the failure of some small branch flows and the inefficiency of fluid passage through the root-like branching structure, the topology designed based on the biomimetic structure of marine organisms and tree roots shapes is not suitable for high Reynolds numbers (Re = 1412 in this study). Conversely, at lower Reynolds numbers (Re = 200 in this study), the topologically optimized structure shows obvious biomimetic phenomena. However, when the Reynolds number is high, the biomimetic phenomena in the TO flow channel most likely be no longer evident.

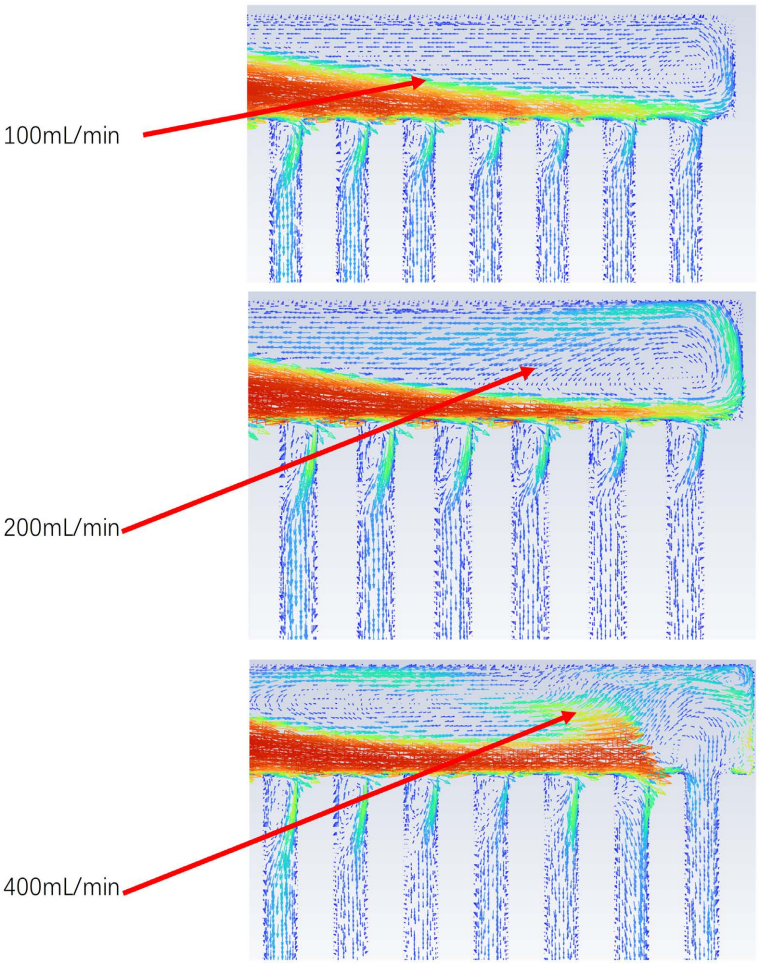

Figure 18. 2 mm microchannel LCP velocity vector of the Z-axis center section.

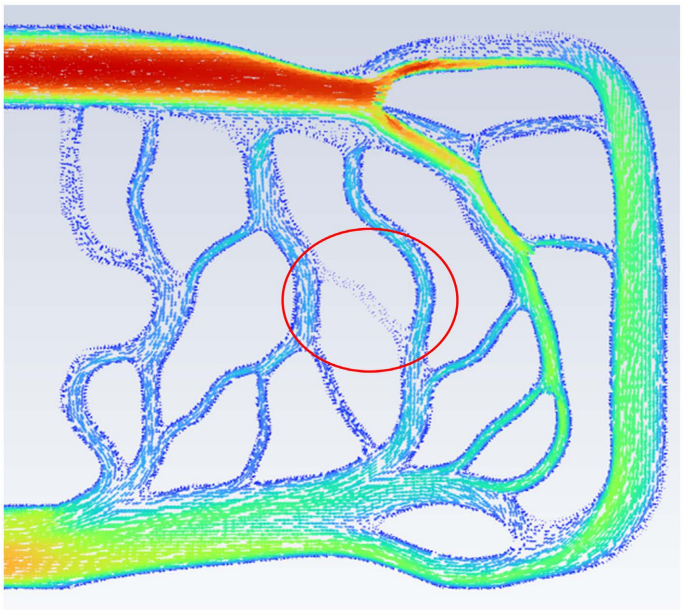

Figure 19. $w_{th} : w_f = 0.5 : 0.5$ TO LCP velocity vector of the Z-axis center section (400 mL/min).

4. Experiment and Results

4.1. Experiment Design

As shown in Figure 4, after stretching the solid part of the w_{th}:w_f = 0.5:0.5 topology flow channel structure in the normal direction by 6 mm, the top and bottom are sealed to form the LCP. The top cover is connected to the main body with screws, and a matching rubber seal ring is used for sealing. Brass connectors are used at the inlet and outlet to connect the water pipes, and waterproof and pressure-resistant sealing tape is applied to the threaded part of the joints.

The TO LCP and 2 mm microchannel LCP are then CNC processed, the processed material is Al6063, connected to the brass connector, to obtain the main body of the LCP in Figure 20, The black rubber ring seals the LCP to prevent water leakage.

The assembled two LCP are performed to thermal performance testing and inlet/outlet pressure drop testing. The experimental test schematic is shown in Figure 21, and the corresponding equipment and instruments are referenced in Table 3. The experiment can adjust and control the flow rate of water in the circulation loop by adjusting the knob of the float flowmeter. The power output of the DC power supply 1 is adjusted to make the power consumption of the ceramic heating heat source equal to the design TDP. The contact interface between ceramic heat source and the LCP were filled with Shin-Etsu X-23-7868-2D thermal grease. The cooling system includes fans and radiators, and the fan air flow rate is adjusted by adjusting the output voltage of the DC power supply 2 to achieve a constant inlet liquid water temperature T_{in} of the LCP.

4.2. Experiment Results

CASE1 and CASE2 Temperature Test Results

After the temperature test in the condition of CASE1 and CASE2 (refers to Table 1), the temperature rise curves were shown in Figure 22. Under CASE1 (66 mL/min, 50W, T_{in} is 25˚C), the cooling system can very accurately control the temperature of the inlet water T_{in} to 25˚C, with a difference of no more than 0.1˚C. In the first 2 minutes, the temperature soars significantly, from 25˚C to a nearly stable temperature, and the whole process time from the start of the test

Figure 20. CNC processed 2 mm microchannel and TO channel LCPs.

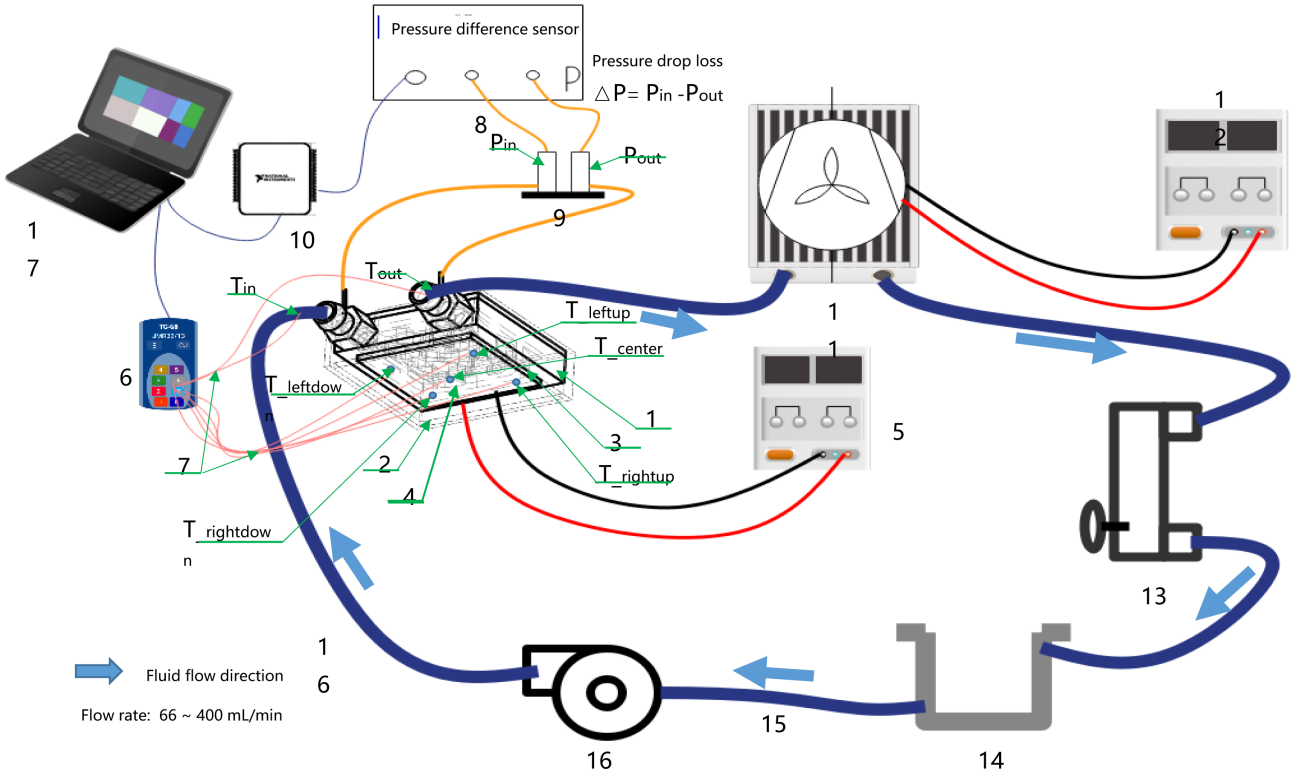

Figure 21. Schematic diagram of the experiment setup.

Table 3. Equipment list for experimental testing device.

NO.	Equipment	Model	Remarks
1	LCP	/	With Intel platform backplate and Clips for installation
2	Aerogel	Thermal conductivity 0.018 W/m·K	Adiabatically insulate the outer surface of the LCP
3	Thermal grease	Shin-Etsu X-23-7868-2D	/
4	Heat source	/	Alumina ceramic as a CPU dummy heater
5	DC power supply 1	WPS305B	Provide power to the heat source
6	Thermocouple data logger	PICO TC-08	Collect and record temperature data
7	Thermocouple wire	OMEGA TT-T-30	With plugs
8	Pressure difference sensor	0-300Pa, 0-10V	Barometric pressure sensor
9	Pressure measuring cylinder	Two PMMA cylindrical structures	Convert the hydraulic pressure to air pressure
10	DAQ device	NI USB-6009	Collecting pressure sensor data
11	Cooling system	Fans and radiators	Cooled the water cycle and obtain constant T_{in}
12	DC power supply 2	HYELEC HY3005MT	Provide power to the cooling system FAN
13	Float flowmeter	LZM4-T	Range 50 - 500 mL/min
14	Water tank	/	/
15	Water pipe	/	/
16	Pump	JT-280	Head max 3 m, q_V max 240 L/H
17	Computer		

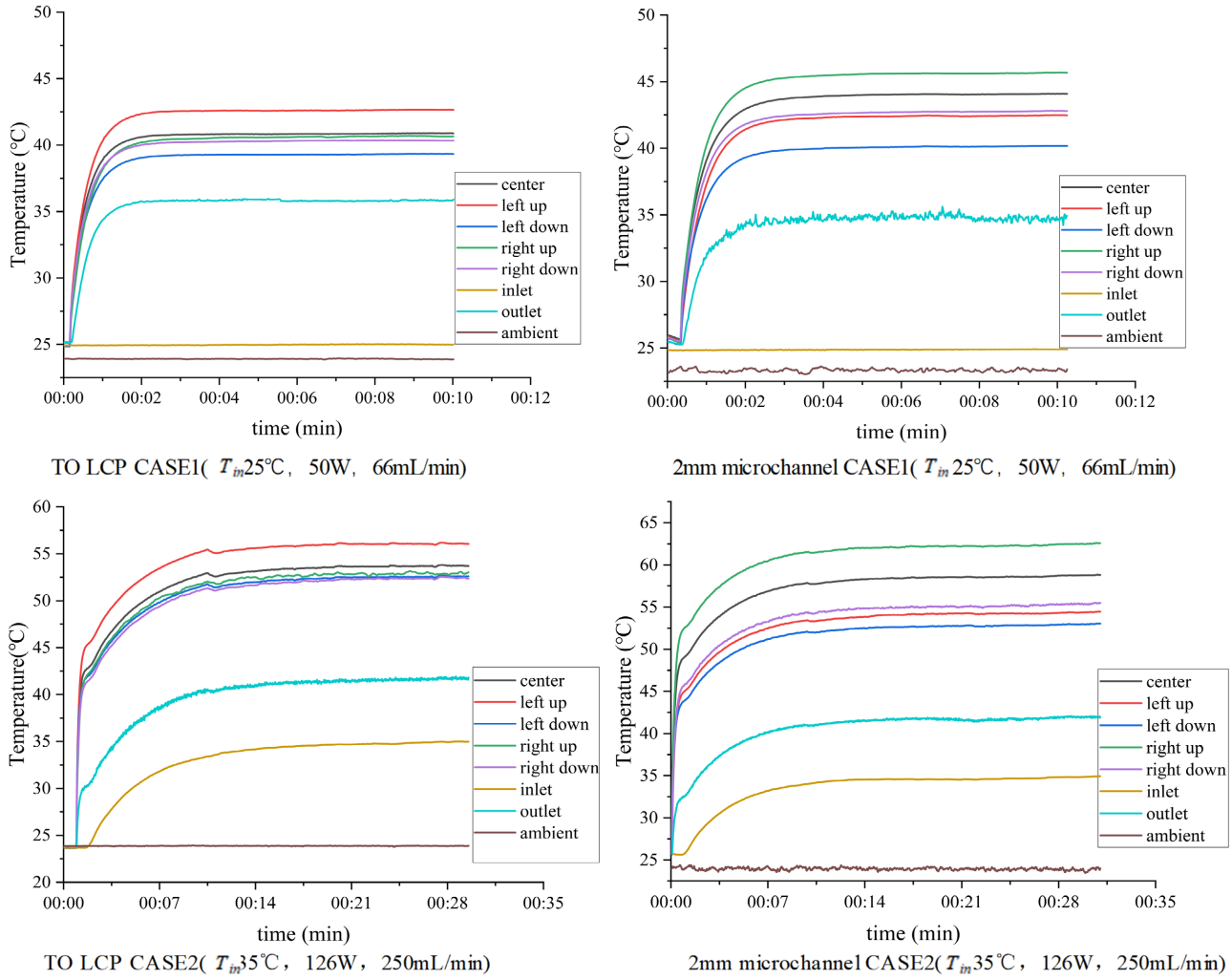

Figure 22. Temperature rise curves for the two kinds of LCP under CASE1 and CASE2 experiment.

to the thermal equilibrium is less than 10 minutes. Under CASE2 (250 mL/min, 126 W, T_{in} is 35˚C), the cooling system can also control the temperature of T_{in} to 35˚C, the temperature soars remarkably In the first 8 minutes, and the whole process time from the start of the test to the thermal equilibrium is about 30 minutes.

The CFD simulation results were compared to obtain the test data in **Table 4**. For two different structures of liquid cold plates in CASE1, the errors between the temperature of each point obtained by the experimental test and CFD simulation is less than 3%, and the average thermal resistance deviation is less than 1.6%. The maximum thermal resistance deviation is slightly larger, but still less than 5%. It shows that the CFD simulation settings and results in this paper can accurately reflect the actual engineering problems. CFD simulations and experimental tests verify each other.

The temperature distribution of the liquid cold plate with topology is reasonable, and its maximum temperature is at the leftup point of the fluid outlet, and the test data is 41.82˚C. The minimum temperature was at the leftdown point

near the fluid inlet, and the test data was 39.33˚C. For the 2mm microchannel structure, the maximum temperature is 44.83˚C at the rightup point where heat accumulation occurs. The lowest temperature is at the leftdown point near fluid inlet at 39.54˚C. The temperature distribution obtained by the experiment is in good agreement with the previous CFD simulation.

The maximum temperature of the TO liquid cold plate obtained by experimental test is 3.01˚C lower than that of the 2 mm microchannel cold plate, the average temperature is 1.53˚C lower, the average thermal resistance is reduced by 9.2%, and the maximum thermal resistance is reduced by 11.3%.

Comparing the results obtained by the experimental test and by CFD simulation in CASE2, referring to Table 5, except for the leftup point of the 2 mm microchannel LCP, (the error between the leftup point is 6.12%), the other point temperature deviations are less than 2.5%, the average thermal resistance deviation is 3.87%, and the maximum thermal resistance deviation is 2.32%, which are all within the acceptable range.

Similarly, the temperature distribution obtained by the experiment is in good agreement with the CFD simulation results. The maximum temperature of the TO LCP obtained by experimental test is 5.94˚C lower than that of the 2 mm microchannel LCP, the average temperature is 3.24˚C lower, the average thermal resistance is reduced by 14.6%, and the maximum thermal resistance is reduced by 21.7%, TO LCP has the better thermal performance.

Table 4. Temperature test data in CASE1 (66 mL/min, 50 W, T_{in} = 25˚C).

Monitor points	w_{th} = 0.5 TO LCP			2mm microchannel LCP		
	Exp.TEMP. (˚C)	CFD.TEM. (˚C)	Deviation[1]	Exp.TEMP. (˚C)	CFD.TEMP. (˚C)	Deviation
Inlet	25.01	25.00	0.04%	24.95	25.00	0.20%
Center	40.88	40.46	1.03%	43.47	42.34	2.59%
Leftup	42.64	41.82	1.92%	42.06	42.89	1.98%
Leftdown	39.33	39.31	0.06%	39.54	39.85	0.79%
Rightup	40.68	41.18	1.24%	44.83	44.29	1.21%
Rightdown	40.36	39.82	1.34%	41.67	42.07	0.96%
Average	40.78	40.52	0.64%	42.31	42.29	0.06%
Outlet	35.88	36.14	0.73%	34.63	33.66	2.81%
R_{th_avg}[2]	0.31536	0.31036	1.59%	0.34728	0.34580	0.43%
R_{th_max}[3]	0.35260	0.33645	4.58%	0.39760	0.38579	2.97%

Note: 1) deviation = (experiment data-CFD data)/experiment data, absolute value. Exp.TEMP refers to experiment temperature; 2) Take the average temperature of the center, leftup, leftdown, rightup and rightdown points and calculated according to Equation (25); 3) Take the maximum temperature of the above five points, and calculated according to Equation (26).

4.3. Multi-Flow Rate CASEs Thermal Test Results

The thermal resistance curve is shown in Figure 23 and Figure 24, and it can be seen that:

(1) For two different structures of LCPs, the deviation between the average thermal resistance obtained by experimental test and by CFD simulation is very little, the maximum deviation of the 2 mm channel liquid cold plate is 2.1%, the deviation of the TO liquid cold plate is slightly larger at high flow, and the deviation is 8.4% at the flow rate of 200 mL/min, but it is still within the acceptable range; The deviation between the maximum thermal resistance obtained by the experimental test and by CFD simulation is also very little, there is a slight deviation at low flow, when the flow rate is 100 mL/min, the deviation of the topology is

Table 5. Temperature test data in CASE2 (250 mL/min, 126 W, T_{in} = 35˚C).

Monitor points	w_{th} = 0.5 TO LCP			2 mm microchannel LCP		
	Exp.TEMP. (˚C)	CFD.TEMP. (˚C)	Deviation	Exp.TEMP. (˚C)	CFD.TEMP. (˚C)	Deviation
Inlet	34.99	35.00	0.03%	35.01	35.00	0.03%
Center	53.91	55.16	2.32%	59.14	58.21	1.57%
Leftup	56.31	56.31	0.00%	54.96	58.33	6.12%
Leftdown	52.68	53.63	1.80%	52.96	53.37	0.78%
Rightup	53.41	54.73	2.47%	62.25	61.61	1.03%
Rightdown	52.49	52.66	0.32%	55.68	55.71	0.05%
Average	53.76	54.50	1.37%	57.00	57.44	0.78%
Outlet	41.83	42.50	1.60%	41.43	42.39	2.31%
R_{th_avg}	0.14897	0.15474	3.87%	0.17451	0.17813	2.08%
R_{th_max}	0.16921	0.16913	0.04%	0.21619	0.21117	2.32%

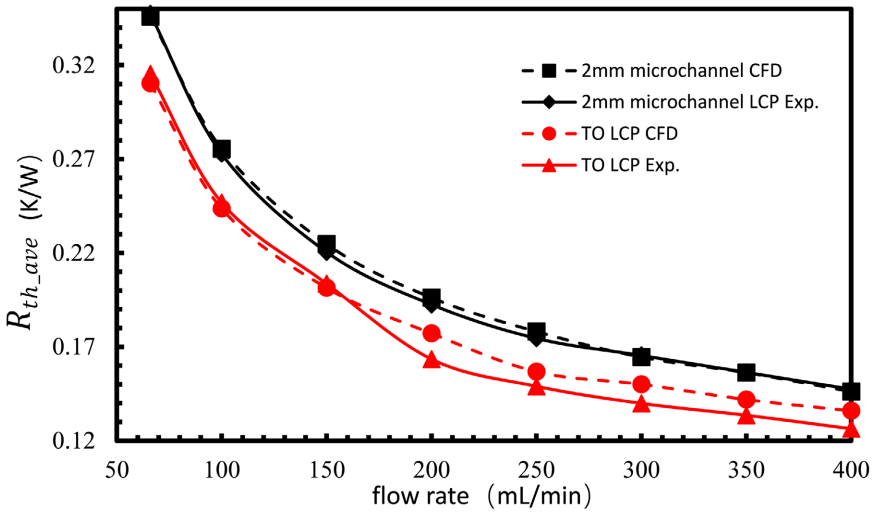

Figure 23. Average thermal resistance curves of the two LCPs.

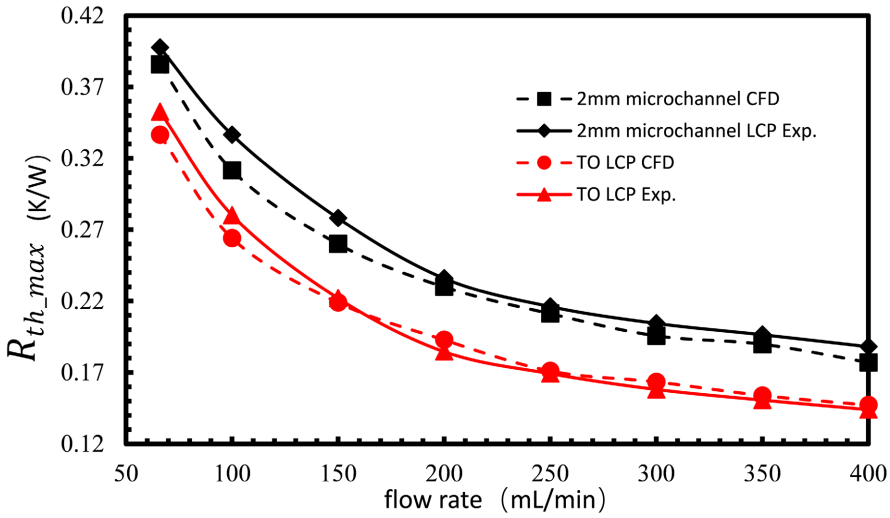

Figure 24. Maximum thermal resistance curves of two LCPs.

5.8%, and the deviation of the 2 mm channel liquid cold plate is 7.4%. It shows that the CFD simulation settings and results in this paper can accurately reflect the actual engineering problems.

2) Under various flow conditions, regardless of experimental test or CFD simulation, the maximum thermal resistance and average thermal resistance of TO structure LCP are less than that of the 2 mm microchannel structure LCP. At high flow rates (300 - 400 mL/min), the maximum thermal resistance was reduced by more than 23% and the average thermal resistance was reduced by more than 14.2%.

Pressure Drop Test

Under Multi-flow rate CASEs, the pressure drop loss of the TO LCP and the 2 mm microchannel LCP was tested and compared with the results CFD simulation results, resulting in the flow resistance curves shown in **Figure 25**.

1) The CFD simulation results of inlet and outlet pressure drop loss of the LCP at various flow rates coincide with the actual experiment test results. At low flow rates, the deviation between the test data and the simulation data is relatively slightly large, with a maximum deviation of 9% (for the 2 mm microchannel LCP at 100 mL/min). This deviation decreases as the flow rate increases, with a minimum deviation of 0.26% (for the TO LCP at 300 mL/min). The pressure difference of the LCPs obtained from the simulation results in this paper accurately reflects the application situation in practical engineering.

2) Through CFD simulation and experiment testing, the trend is the same: at the low flow rate of 66 mL/min, the pressure drop between the topology and the 2 mm microchannel structure is close, and the difference is very little (the simulation and experiment pressure results are less than 0.7%). However, when the flow rate gradually increases, the pressure drop loss of the 2 mm microchannel liquid cold plate gradually increases compared with the topology optimization LCP, and the larger the flow rate, the more obvious this trend is, at the flow rate

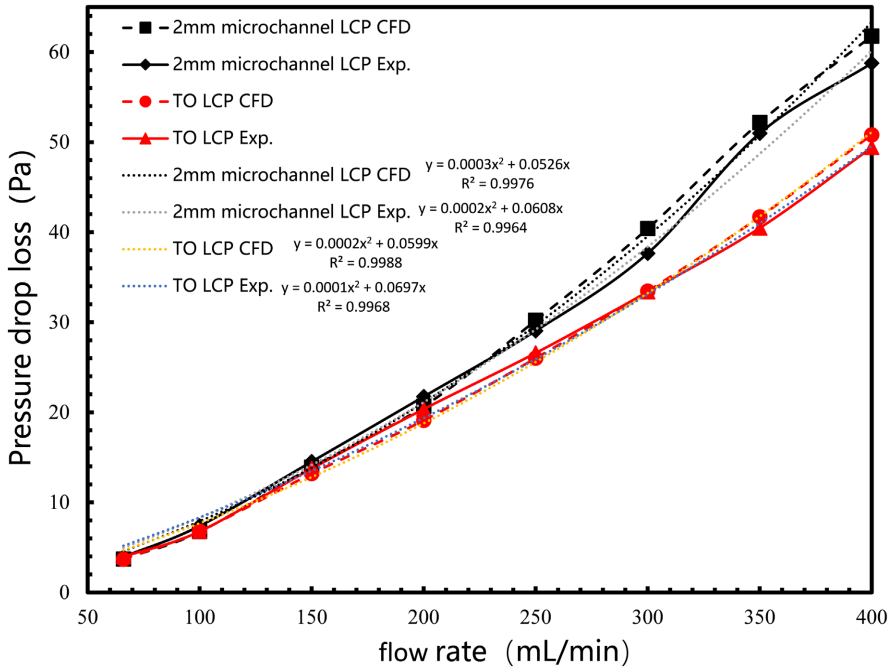

Figure 25. CFD and Experiment Flow resistance curves of the two LCPs.

of 400 mL/min, the pressure drop loss of the simulated 2 mm microchannel LCP is 22% larger than that of the topology optimization LCP, and the pressure loss of the tested 2 mm microchannel liquid cold plate is 19% larger than that of the topology optimized liquid cold plate. Referring to the conclusion of Section 3.5.2, this is due to the fact that the higher the flow rate of the 2 mm microchannel LCP, the more increase in its backflow and vortices leaded to an increase in energy loss.

3) for the topology optimization LCP, the flow resistance curve equation obtained by the test is $y = 0.0001x^2 + 0.0697x$ ($R^2 = 0.9968$, x refers to the flow rate, y refers to pressure drop loss), and obtained by simulation optimization is $y = 0.0002x^2 + 0.0599x$ ($R^2 = 0.9988$), and its resistance coefficient is smaller than that of the 2 mm microchannel liquid cold plate, which can be used to calculate the pressure loss of the LCP under other flow rates and guide the selection of the pump and liquid cooling system matching the LCP.

4) According to the flow resistance curve function obtained from CFD simulation and experimental, as the flow rate increases, the pressure difference increases in a quadratic polynomial proportion and the thermal resistance decreases. However, at higher flow rates, the microchannel structure is prone to backflow and vortex phenomenon. Additionally, at higher flow rates, some branch-like flow in the topology channel tends to bypass and become ineffective. When the flow rate reaches a certain level, the pressure difference increases sharply, and the trend of decreasing thermal resistance becomes less apparent. Increasing the flow rate does not yield an economically viable thermal solution. The LCP in this study, validated through simulation and experiments, is suitable for flow conditions below 400 mL/min. Based on the thermal resistance curve

and flow resistance curve, processors from the Xeon E5 series and Xeon D series are selected that can accommodate the existing Intel 52.5 mm * 45 mm CPU package architecture.

5. Conclusions

In this paper, a mathematical model for the topology optimization design is established for the LCP of the Intel Xeon 52.5 mm * 45 mm CPU package architecture, and 2D topology optimization configurations of the LCP with different objective weighting factors are obtained. Then, the 3D structure of the LCP is designed. A series of physical and numerical experiments are carried out to investigate the thermal performance, pressure drop and the internal flow structures under various working conditions of the LCPs with different channels. The main conclusions are as follows.

- When the weighting factor of the heat dissipation objective w_{th} is small (with the pressure drop dissipation objective weight being large), the channels optimized through topology have a larger cross-section and fewer branches, resulting in a relatively uneven temperature distribution but lower pressure drop loss. As w_{th} increases, the optimized channels become smaller and more extensively distributed. The temperature becomes more uniform, but the pressure drop loss increases. Therefore, when choosing the best structure, balance thermal performance and pressure drop.
- Bio-mimicry is more noticeable at low *Re* numbers in the topology optimization channel structure but less so at high *Re* numbers.
- In topology optimization LCP, the temperature distribution is more uniform, with better heat dissipation performance and lower pressure drop loss compared to traditional LCP. Compared to traditional serpentine channels, the topology optimization channel shows a 26.9% reduction in maximum thermal resistance, a 40.9% increase in Nusselt number, and a 51.3% decrease in pressure loss; Compared to 1 mm straight microchannels, the maximum temperature remains comparable, the Nusselt number can increase by 33.8%, and the pressure drop decreases by 39.9%. Compared to 2 mm straight microchannels, the maximum thermal resistance decreases by 23%, the Nusselt number can increase by 76.1%, and the pressure drop decreases by over 20%. Therefore, the topology-optimized LCP can significantly improve the performance of data center CPUs with lower energy consumption.
- As flow rates rise, LCP pressure drop increases in a quadratic function, while thermal resistance decreases. However, microchannels are prone to backflow and vortices, and topology-optimized channels may have flow issues. When flow reaches a threshold, pressure drop sharply rises while thermal resistance slightly decreases. Further, increasing flow rates are not cost-effective for thermal solutions.

In the future, as data center server CPUs are upgraded, CPUs will have larger TDP and higher heat flux density. For instance, Intel's latest XEON Scalable 5th

generation CPU requires topology optimization of corresponding LCPs at even higher Reynolds numbers and higher thermal conductivity. However, conducting fluid-solid-thermal coupled topology optimization calculations at higher Reynolds numbers or even turbulent conditions incur extremely high computational and time costs, and are highly susceptible to numerical instability. This poses a challenge to the research of topology optimization and requires further exploration by scholars in subsequent work.

Conflicts of Interest

The authors declare no conflicts of interest regarding the publication of this paper.

References

[1] The Green Grid (2008) Center Power Efficiency Metrics: PUE and DCiE. https://www.missioncriticalmagazine.com/ext/resources/MC/Home/Files/PDFs/TGG_Data_Center_Power_Efficiency_Metrics_PUE_and_DCiE.pdf

[2] Hnayno, M., Chehade, A.A., Klaba, H., Bauduin, H., Polidori, G. and Maalouf, C. (2022) Performance Analysis of New Liquid Cooling Topology and Its Impact on Data Centres. *Applied Thermal Engineering*, **213**, Article 118733. https://doi.org/10.1016/j.applthermaleng.2022.118733

[3] Bao, Y., Chen, J. and Shao, S. (2023) Research Status of High-Efficient Liquid Cooling Technology in Data Center. *Refrigeration and Air-Conditioning*, **23**, 58-69.

[4] Qiu, Y., Hu, W., Wu, C. and Chen, W. (2020) An Experimental Study of Microchannel and Micro-Pin-Fin Based On-Chip Cooling Systems with Silicon-to-Silicon Direct Bonding. *Sensors*, **20**, Article 5533. https://doi.org/10.3390/s20195533

[5] Maxwell, J.C. (1864) XLV. On Reciprocal Figures and Diagrams of Forces. *The London, Edinburgh, and Dublin Philosophical Magazine and Journal of Science*, **27**, 250-261. https://doi.org/10.1080/14786446408643663

[6] Michell, A.G.M. (1904) LVIII. The Limits of Economy of Material in Frame-Structures. *The London, Edinburgh, and Dublin Philosophical Magazine and Journal of Science*, **8**, 589-597. https://doi.org/10.1080/14786440409463229

[7] Dorn, W.C., Gomory, R.E. and Grenberg, H. (1964) Automatic Design of Optimal Structures. *Journal de Mecanique*, **3**, 25-52.

[8] Cheng, K.T. and Olhoff, N. (1981) An Investigation Concerning Optimal Design of Solid Elastic Plates. *International Journal of Solids and Structures*, **17**, 305-323. https://doi.org/10.1016/0020-7683(81)90065-2

[9] Bendsøe, M.P. (1989) Optimal Shape Design as a Material Distribution Problem. *Structural Optimization*, **1**, 193-202. https://doi.org/10.1007/BF01650949

[10] Zhou, M. and Rozvany, G.I. (1991) The COC Algorithm, Part II: Topological, Geometrical and Generalized Shape Optimization. *Computer Methods in Applied Mechanics and Engineering*, **89**, 309-336. https://doi.org/10.1016/0045-7825(91)90046-9

[11] Mlejnek, H.P. and Schirrmacher, R. (1993) An Engineer's Approach to Optimal Material Distribution and Shape Finding. *Computer Methods in Applied Mechanics and Engineering*, **106**, 1-26. https://doi.org/10.1016/0045-7825(93)90182-W

[12] Joo, Y., Lee, I. and Kim, S.J. (2017) Topology Optimization of Heat Sinks in Natural

Convection Considering the Effect of Shape-Dependent Heat Transfer Coefficient. *International Journal of Heat and Mass Transfer*, **109**, 123-133. https://doi.org/10.1016/j.ijheatmasstransfer.2017.01.099

[13] You, H. (2018) Topology Optimization of Cooling Structures for Electronics Devices. Doctoral Dissertation, Shanghai Jiao Tong University, Shanghai.

[14] Khan, U.A., Ullah, H. and Nawaz, A. (2023) Design and Optimization of Heatsink for an Active CPU Cooler Using Numerical Simulations. *Journal of Advanced Research in Fluid Mechanics and Thermal Sciences*, **111**, 214-224. https://doi.org/10.37934/arfmts.111.2.214224

[15] Borrvall, T. and Petersson, J. (2003) Topology Optimization of Fluids in Stokes Flow. *International Journal for Numerical Methods in Fluids*, **41**, 77-107. https://doi.org/10.1002/fld.426

[16] Evgrafov, A. (2005) The Limits of Porous Materials in The Topology Optimization of Stokes Flows. *Applied Mathematics and Optimization*, **52**, 263-277. https://doi.org/10.1007/s00245-005-0828-z

[17] Dede, E.M. (2009) Multiphysics Topology Optimization of Heat Transfer and Fluid Flow Systems. *Proceedings of the COMSOL Users Conference*, Boston, 30 March 2009.

[18] Yoon, G.H. (2010) Topological Design of Heat Dissipating Structure with Forced Convective Heat Transfer. *Journal of Mechanical Science and Technology*, **24**, 1225-1233. https://doi.org/10.1007/s12206-010-0328-1

[19] Matsumori, T., Kondoh, T., Kawamoto, A. and Nomura, T. (2013) Topology Optimization for Fluid-Thermal Interaction Problems under Constant Input Power. *Structural and Multidisciplinary Optimization*, **47**, 571-581. https://doi.org/10.1007/s00158-013-0887-8

[20] Koga, A.A., Lopes, E.C.C., Nova, H.F.V., De Lima, C.R. and Silva, E.C.N. (2013) Development of Heat Sink Device by Using Topology Optimization. *International Journal of Heat and Mass Transfer*, **64**, 759-772. https://doi.org/10.1016/j.ijheatmasstransfer.2013.05.007

[21] Wei, X. and Ding, X. (2017) Adaptive Topology Optimization of Heat Transfer Structure by Optimality Criteria. *Journal of Mechanical Engineering*, **53**, 153-160. https://doi.org/10.3901/JME.2017.20.153

[22] Cui, W. (2017) Optimization of Heat Transfer Structure Considering Fluid-Solid Coupling. Doctoral Dissertation, Dalian University of Technology, Dalian.

[23] Hu, S. (2018) Study on Fluid Topology Optimization Method Based on Variable Density Method and Experimental Analysis. Doctoral Dissertation, Xiangtan University, Xiangtan.

[24] Li, H., Ding, X., Meng, F., Jing, D. and Xiong, M. (2019) Optimal Design and Thermal Modelling for Liquid-Cooled Heat Sink Based on Multi-Objective Topology Optimization: An Experimental and Numerical Study. *International Journal of Heat and Mass Transfer*, **144**, Article 118638. https://doi.org/10.1016/j.ijheatmasstransfer.2019.118638

[25] Chen, J.B. (2021) Topology Optimization Design and Experimental Investigation of Cooling Channel for Heat Exchanger. Doctoral Dissertation, Xidian University, Xi'an.

[26] Zhao, X., Zhou, M. and Sigmund, O. (2017) A "Poor Man's Approach" to Topology Optimization of Cooling Channels Based on a Darcy Flow Model. *International Journal of Heat and Mass Transfer*, **116**, 1108-1123. https://doi.org/10.1016/j.ijheatmasstransfer.2017.09.090

[27] An, Li. (2020) Topology Optimization of Fluid-Solid Conjugate Heat Transfer Structure. Doctoral Dissertation, Dalian University of Technology, Dalian.

[28] Han, S. (2021) Optimal Design of Cooling Flow Channels Based on Fluid-Solid Conjugate Heat Transfer. Doctoral Dissertation, Dalian University of Technology, Dalian.

[29] Wang, Y.Y., Yan, K., Cai, X.H., Pan, Y., Sun, G., *et al.* (2022) Topology Optimization of Simplified Convective Heat Transfer Problem by COMSOL. *Chinese Journal of Computational Mechanics*. https://kns.cnki.net/kcms/detail/21.1373.o3.20220728.1514.046.html

[30] Mo, X.B., Zhi, H., Xiao, Y.Z., Hua, H.Y. and He, L. (2021) Topology Optimization of Cooling Plates for Battery Thermal Management. *International Journal of Heat and Mass Transfer*, **178**, Article 121612. https://doi.org/10.1016/j.ijheatmasstransfer.2021.121612

[31] Chen, F., Wang, J. and Yang, X. L. (2022) Topology Optimization Design and Numerical Analysis on Cold Plates for Lithium-Ion Battery Thermal Management. *International Journal of Heat and Mass Transfer*, **183**, Article 122087. https://doi.org/10.1016/j.ijheatmasstransfer.2021.122087

[32] Chen, F. (2022) Study on Topology Optimization Design of Cold Plate Channel in Battery Thermal Management System. Doctoral Dissertation, Jiangsu University of Science and Technology, Zhenjiang.

[33] Wu, M.S. (2023) Multi-Objective Topology Optimization of Cold Plates Featuring Branched and Streamlined Mini-Channels for Thermal Management System of Lithium-Ion Battery Module. *Journal of Energy Storage*, **72**, Article 108362. https://doi.org/10.1016/j.est.2023.108362

[34] Wang, Y., Xuan, Q.D., Peyman, G.Z. and Chung, J.D. (2023) Liquid-Cooled Cold Plate for a Li-Ion Battery Thermal Management System Designed by Topology Optimization. *Journal of Mechanical Science and Technology*, **37**, 2079-2086. https://doi.org/10.1007/s12206-023-0343-7

[35] Malawski, M., Figiela, K., Gajek, A. and Zima, A. (2018) Benchmarking Heterogeneous Cloud Functions. In: Heras, D., *et al.*, Eds., *Euro-Par* 2017: *Parallel Processing Workshops. Euro-Par* 2017. *Lecture Notes in Computer Science*, Vol. 10659, Springer, Cham, 415-426. https://doi.org/10.1007/978-3-319-75178-8_34

[36] Figiela, K., Gajek, A., Zima, A., Obrok, B. and Malawski, M. (2018) Performance Evaluation of Heterogeneous Cloud Functions. *Concurrency & Computation: Practice & Experience*, **30**, e4792. https://doi.org/10.1002/cpe.4792

[37] (2012) [The New Intel Xeon E5-2600 Series Processors Employ an LSI SAS Solution]. *Computer & Network*, No. 6, 76.

[38] Huang, J., Li, G.G., Hou, Q.G. and Zhao, K. (2020) Total Cost of Ownership Modeling Method for Cloud Computing of Traffic. *Journal of Harbin Engineering University*, **41**, 589-594.

[39] Intel (2024) Intel® Xeon® D Processors. https://www.intel.com

[40] Intel (2018) Intel® Xeon® Processor E5 V4 Product Family—Thermal Mechanical Specification and Design Guide. Intel, California. http://www.intel.com/design/literature.htm

[41] Haertel, J., Engelbrecht, K., Lazarov, B.S. and Sigmund, O. (2015) Topology Optimization of Thermal Heat Sinks. *Proceedings of the COMSOL Conference* 2015, Grenoble, 14-16 October 2015.

[42] Intel (2022) Green Data Center Innovation Practice Liquid Cooling Cold Plates De-

sign Reference Single Page 0822 Solution Book.

[43] Olesen, L.H., Okkels, F. and Bruus, H. (2006) A High-Level Programming-Language Implementation of Topology Optimization Applied to Steady-State Navier-Stokes Flow. *International Journal for Numerical Methods in Engineering*, **65**, 975-1001.

[44] Kawamoto, T., Matsumori, S., Yamasaki, T., Nomura, T., Kondoh, S. and Nishiwaki. (2011) Heaviside Projection Based Topology Optimization by a PDE-Filtered Scalar Function. *Structural and Multidisciplinary Optimization*, **44**, 19-24. https://doi.org/10.1007/s00158-010-0562-2

[45] Lazarov, B.S. and Sigmund, O. (2011) Filters in Topology Optimization Based on Helmholtz-Type Differential Equations. *International Journal of Numerical Methods in Engineering*, **86**, 765-781. https://doi.org/10.1002/nme.3072

[46] Wang, F., Lazarov, B.S. and Sigmund, O. (2011) On Projection Methods, Convergence and Robust Formulations in Topology Optimization. *Structural and Multidisciplinary Optimization*, **43**, 767-784. https://doi.org/10.1007/s00158-010-0602-y

[47] Landau, L.D. and Lifshitz, E.M. (2000) Course of Theoretical Physics: Fluid Mechanics, Vol. 6. 2nd Edition, Butterworth and Heinemann, Oxford.

[48] COMSOL (2020) Optimization of a Tesla Microvalve. COMSOL, Stockholm. https://www.comsol.com/model/optimization-of-a-tesla-microvalve-14513

[49] Boggs, P.T. and Tolle, J.W. (2008) Sequential Quadratic Programming. *Acta Numerica*, **4**, 1-51. https://doi.org/10.1017/S0962492900002518

[50] COMSOL Multiphysics Reference Manual V. 6.0, Stockholm, 2021.

[51] Zhou, W.N., Sun, Q., Guan, S.L., *et al.* (2021) Liquid Flow and Heat Transfer Characteristics of Liquid Cooling Plate with Hollow-Fin. *Journal of Energy Conservation*, **9**, 506-512. https://doi.org/10.3969/j.issn.2095-560x.2021.06.007

[52] Farhan, M., Amjad, M., Anwar, Z., Arslan, M., Mujtaba, A., Riaz, F., *et al.* (2022) Design and Analysis of Liquid Cooling Plates for Different Flow Channel Configurations. *Thermal Science*, **26**, 1463-1475. https://doi.org/10.2298/TSCI201111196F

[53] Ye, J., Aldaher, A.Y.M. and Tan, G. (2023) Thermal Performance Analysis of 18,650 Battery Thermal Management System Integrated with Liquid-Cooling and Air-Cooling. *Journal of Energy Storage*, **72**, Article 108766. https://doi.org/10.1016/j.est.2023.108766